

Original Research Article

Coupling dynamics of 2D Notch-Delta signalling

Francisco Berkemeier ^{a,*}, Karen M. Page ^b^a Department of Pathology, University of Cambridge, UK^b Department of Mathematics and IPLS, University College London, UK

ARTICLE INFO

Keywords:

Notch
Signalling
Stability
Protrusions
Lateral inhibition

ABSTRACT

Understanding pattern formation driven by cell-cell interactions has been a significant theme in cellular biology for many years. In particular, due to their implications within many biological contexts, lateral-inhibition mechanisms present in the Notch-Delta signalling pathway led to an extensive discussion between biologists and mathematicians. Deterministic and stochastic models have been developed as a consequence of this discussion, some of which address long-range signalling by considering cell protrusions reaching non-neighbouring cells. The dynamics of such signalling systems reveal intricate properties of the coupling terms involved in these models. In this work, we investigate the advantages and drawbacks of a single-parameter long-range signalling model across diverse scenarios. By employing linear and multi-scale analyses, we discover that pattern selection is not only partially explained but also depends on nonlinear effects that extend beyond the scope of these analytical techniques.

1. Introduction

In epithelial tissue, depending on the nature of the contact between cells, the Notch-Delta signalling pathway leads to fundamentally different patterns [1–3]. In highly packed epithelial layers, some cells have the ability to create extensions of themselves, developing protrusions that reach non-neighbouring cells and yielding a new and fundamental factor in the signalling dynamics. These basal actin-based filopodia are elongated and oriented in different directions, extending signalling to second or third neighbour cells [4–8].

In recent years, long-range signalling via filopodia has been shown to significantly impact the distribution and sparse patterning of sensory organ precursor (SOP) cells in the fly notum [9–11]. In other work, spatiotemporal patterns of spinal neuron differentiation were revealed to be mediated by basal protrusions [12]. In contrast to the frequently observed short-ranged patterns induced by short-range signalling, cell protrusions result in sparser SOP cell patterning.

The stochastic nature of these biological systems crucially affects patterning. For example, noise arising from dynamic protrusions has been shown to have a significant role in pattern refinement when studying the organisation of bristles on the *Drosophila melanogaster* notum [9]. A cellular automaton model of cell-cell signalling revealed that rule-dependent structured noise also triggers refined and biased patterning [10], hinting at the self-organising nature of such systems. Intrinsic noise, driven by stochastic gene expression, has been studied via the Chemical Langevin Equation [13] and shown to directly affect juxtacrine-based pattern formation [14].

In addition to constructing realistic long-range signalling models capable of numerically describing long-range patterning, linear stability analysis (LSA) has revealed inherent characteristics of lateral inhibition models [15–17]. Biased and long-range signalling was also studied in [18], where weight-based coupling functions were considered for several one-dimensional signalling systems. We aim to partially extend this work by studying the two-dimensional hexagonal array under specific signalling weights.

In 1996, Joanne Collier and colleagues developed the first model of Notch-mediated lateral inhibition [19]. In this work, the authors considered purely juxtacrine signalling dynamics, where the signalling cell and the target cell are in direct physical contact. We define a model of long-range Notch-Delta signalling, which is a relative weight-based extension of the original Collier model, and name it the ϵ -Collier model. We introduce a weighting parameter ϵ that relatively weights juxtacrine and long-range signalling contributions, creating a complex non-local signalling network.

Under different filopodium behaviour and lifespan assumptions, one can explore the robustness of the extended Collier model via LSA, providing a general framework for analysing autonomous systems of signalling cells, as detailed in Supplementary Note 1 (SN1). Furthermore, such a parameterised model allows us to investigate the limits on cell coupling sufficient to obtain long-range patterns. In parallel, we explore the effects of stochastic filopodium dynamics on patterning. Finally, we expand some of the techniques from LSA to describe a general framework for multiple-scale methods and weakly nonlinear

* Correspondence to: Department of Pathology, University of Cambridge, 10 Tennis Court Road, Cambridge, CB2 1QP, UK.
E-mail address: fp409@cam.ac.uk (F. Berkemeier).

stability analysis (WNSA) of coupled and decoupled dynamical systems (SN2).

In this paper, we first present the Collier model of Notch-Delta signalling, followed by its extension to long-range signalling, which we call the ϵ -Collier model. We then perform a linear stability analysis of this system. The results of the LSA are compared with numerical simulations. The cases of longer/oriented protrusions and stochastic protrusions are analysed. In the latter case, we assume that protrusions link and unlink at random. Stochastic protrusions can lead to pattern refinement over time. We perform a numerical bifurcation analysis of the ϵ -Collier model, showing which modes are expected to grow near a bifurcation, and show that these accurately predict the results of numerical simulations there. Finally, we present a multiscale method for analysing weakly nonlinear dynamics, and show that it is difficult to apply to this system.

2. Main methods

2.1. Lateral inhibition

We consider a periodic $N \times M$ hexagonal lattice (hexagonal torus), where each cell has 6 neighbouring cells (see Fig. 1(a)). For a given cell, we assume juxtacrine signalling occurs with all 6 of its neighbours via the usual Collier model [19]. Here, the authors used experimental data to build an ordinary differential equation (ODE) model of the feedback loop between two adjacent cells induced by Notch signalling (lateral inhibition). The model consists of a system of coupled ODEs per cell. Denoting by n_i and d_i the levels of Notch and Delta activity in cell i , we have the following system

$$\frac{d}{dt}n_i = f(\langle d_i \rangle) - n_i \quad (1)$$

$$\frac{d}{dt}d_i = v(g(n_i) - d_i), \quad (2)$$

where $f, g : [0, \infty) \rightarrow [0, \infty)$ are continuous increasing and decreasing functions, respectively, often taken to be Hill functions

$$f(x) = \frac{x^k}{a + x^k} \quad (3)$$

$$g(x) = \frac{1}{1 + bx^h} \quad (4)$$

for $x \geq 0$ and $h, k \geq 1$. $r_t \equiv 1/a$ and b are the trans-interactions strength and ligand inhibition strength parameters, respectively¹. $v > 0$ is the ratio between Notch and Delta decay rates, determining the strength of decay. Finally, $\langle d_i \rangle$ is the average level of Delta activity in the cells adjacent to cell i , that is,

$$\langle d_i \rangle = \frac{1}{|\text{nn}(i)|} \sum_{j \in \text{nn}(i)} d_j, \quad (5)$$

where the sum is taken over the nearest neighbours $\text{nn}(i)$ of cell i and $|\text{nn}(i)|$ is the total number of neighbours. In general, depending on the hexagonal lattice orientation, either N or M must be even to ensure periodicity. From the previous equations, one can see that the rate of production of Notch activity is an increasing function of the level of Delta activity in neighbouring cells. In contrast, the rate of production of Delta activity is a decreasing function of the level of activated Notch within the same cell. The production of Notch and Delta activity is balanced by decay.

¹ The quantity $a^{1/k}$ is the neighbour Delta activity level necessary for half-maximal Notch activation, while $b^{-1/h}$ is the Notch activity level necessary for half-maximal Delta inhibition.

2.2. Long-range signalling

In addition to lateral cell-cell signalling, we also consider the possibility of long-range signalling with respect to non-neighbouring cells. We loosely refer to cell protrusions as the main mechanism for general, isotropic long-range signalling, interchangeably using these terms. A detailed discussion of protrusion dynamics is presented in [20]. For now, our notion of protrusions remains relatively abstract. There are several ways to implement protrusion-cell signalling. As a first simplification, we assume $\langle d_i \rangle$ is the only term affected by long-range signalling and extend its definition to include non-neighbouring cells that contact cell i . We also investigate the cases where ligand density decays with distance and protrusions are stochastic.

In general, we consider the approach suggested in [18]. Here, the authors used a weighting function $\omega(s, r)$ defining the signalling level from a signaller cell s to a receiver cell r . ω determines which cells are connected through protrusions, defining a connectivity matrix whose entries yield the signalling intensity. In a simplistic protrusion model, all non-zero entries of such a matrix are equal. The weighting function ω captures the matrix information, and we may rewrite the interaction term as follows

$$\langle d_i \rangle = \sum_{j \in \text{nn}(i)} \omega(i, j) d_j, \quad (6)$$

where the sum is made over the neighbours of i , $\text{nn}(i)$, and the non-neighbouring cells that are reached by the protrusions, $\text{np}(i)$, of cell i . Such an array of indexes is defined as $\text{n}(i) = \text{nn}(i) \cup \text{np}(i)$. The further assumption that each cell has a finite amount of active ligand to distribute at any given time point results in the following restriction

$$\sum_{j \in \text{n}(i)} \omega(i, j) = \bar{\omega} < +\infty. \quad (7)$$

Although there is some freedom in the interpretation of $\bar{\omega}$, we assume $\bar{\omega} = 1$ for simplicity.

2.3. The ϵ -Collier model

Our model, hereafter named the ϵ -Collier model, extends the mathematical systems in [19] by considering the inclusion of long-range signalling via protrusions balanced by the relative weighting factor $\epsilon \in [0, 1]$. We begin by weighting each signalling contribution, juxtacrine (ω_J) and protrusion-based (ω_P), by the factor ϵ , to define the combined weighting function

$$\omega \equiv (1 - \epsilon)\omega_J + \epsilon\omega_P. \quad (8)$$

Eq. (6)–Eq. (8) define the ϵ -Collier model, considering protrusions of relative signalling intensity ϵ . Naturally, Eq. (8) is only interesting when ω_J and ω_P are restricted to $\text{nn}(i)$ and $\text{np}(i)$, respectively. For example, the case $\epsilon = 0$ and $\omega_J(i, j) = \chi_{\text{nn}(i)}(j)/6$, where $\chi_{\text{nn}(i)}$ is the indicator (or characteristic) function of the set $\text{nn}(i)$, corresponds to the original Collier model.

2.4. Coupling dynamics

We perform a linear stability analysis to understand the criteria for pattern formation driven by Notch-Delta signalling. This is a useful tool to not only identify the regions of the parameter space for which spontaneous patterning of SOP cells occurs but also to determine the typical spacing between Delta-expressing cells, often called the characteristic length of the pattern or pattern wavelength [15,17,19]. Our analysis closely follows the methods outlined in [18,19,21] and Murray [22], for the two-dimensional hexagonal array, and is based on the framework presented in SN1.

Eq. (1)–Eq. (2) possesses a single positive homogeneous steady state (n^*, d^*) . At this state, we have $f(g(n^*)) = n^*$ and $g(n^*) = d^*$, which is unique because $f(g(n))$ is monotonically decreasing for all $n \geq 0$. Then,

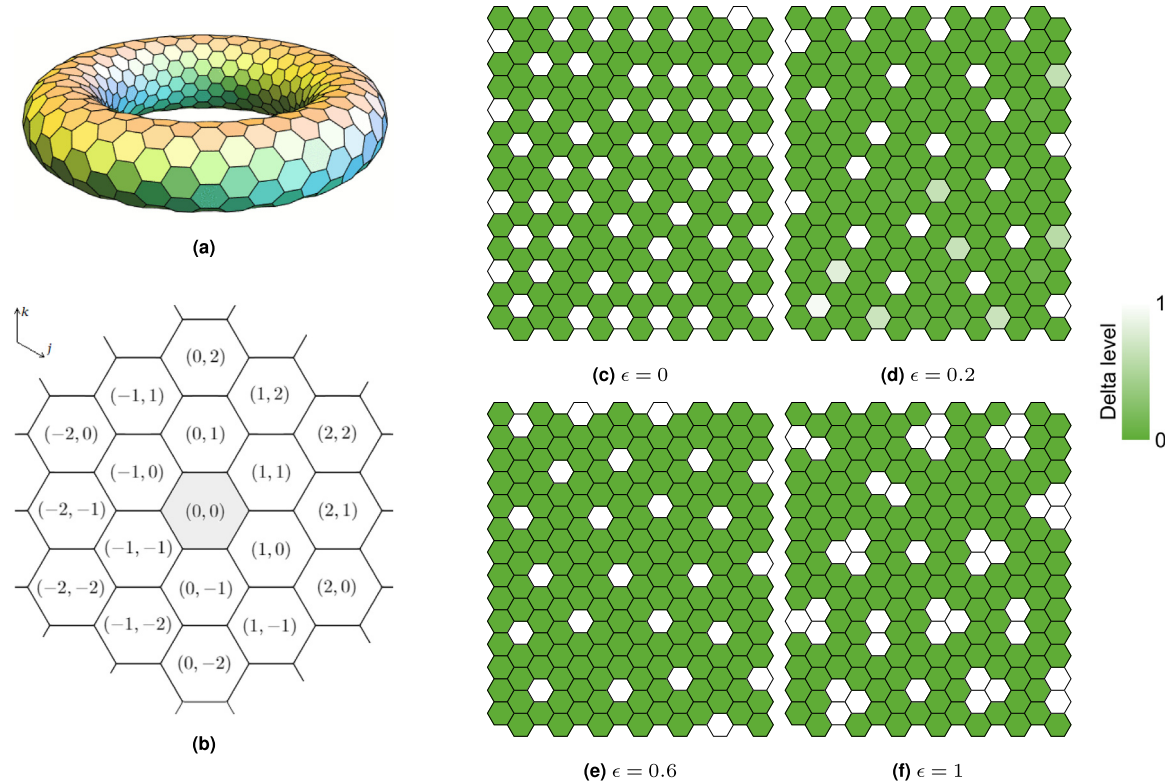


Fig. 1. Long-range Notch-Delta signalling on hexagonal lattices.

(a) Hexagonal torus. Periodic hexagonal lattices can be seen as hexagonal tori. (b) Hexagonal lattice main directions (j, k axes) and cell position indexation relative to a focal cell $(0, 0)$. Different cell labelling schemes yield equivalent formulations of $\Omega_{\bar{q}, \bar{p}}$, as defined in Eq. (17). (c–f) Notch-Delta patterns on a 14×14 periodic lattice for varying ϵ . SOP cells (white, high Delta, low Notch) contrast with non-SOP cells (green, low Delta, high Notch). Here, $h = k = 6$, $a = 10^{-8}$, $b = 10^2$, and $v = 1$. Initial conditions $n_i(0)$ and $d_i(0)$ have arbitrary values close to the homogeneous steady state $(n^*, d^*) \approx (0.744, 0.055)$.

for small perturbations $\tilde{n}_i = n_i - n^*$ and $\tilde{d}_i = d_i - d^*$, linearisation leads to

$$\frac{d}{dt} \tilde{n}_i = A \langle \tilde{d}_i \rangle - \tilde{n}_i \quad (9)$$

$$\frac{d}{dt} \tilde{d}_i = vB \tilde{n}_i - v \tilde{d}_i, \quad (10)$$

where $A = f'(g(n^*))$ is the signal trans-activation by the ligand and $B = g'(n^*)$ is the ligand inhibition by the signal. For a $N \times M$ periodic hexagonal lattice, with $1 \leq j \leq N$ and $1 \leq k \leq M$, the perturbations can be written as a discrete Fourier series

$$\tilde{n}_i \equiv \tilde{n}_{j,k} = \sum_{q=1}^N \sum_{p=1}^M \xi_{q,p} e^{2\pi i(qj/N + pk/M)} \quad (11)$$

$$\tilde{d}_i \equiv \tilde{d}_{j,k} = \sum_{q=1}^N \sum_{p=1}^M \eta_{q,p} e^{2\pi i(qj/N + pk/M)}, \quad (12)$$

where two subindexes have been used to refer to the spatial position of cell i within the two-dimensional hexagonal lattice (see Fig. 1(b)). For $1 \leq q \leq N$ and $1 \leq p \leq M$, the inverted transform is

$$\xi_{q,p} = \frac{1}{MN} \sum_{k=1}^M \sum_{j=1}^N \tilde{n}_{j,k} e^{-2\pi i(qj/N + pk/M)} \quad (13)$$

$$\eta_{q,p} = \frac{1}{MN} \sum_{k=1}^M \sum_{j=1}^N \tilde{d}_{j,k} e^{-2\pi i(qj/N + pk/M)}. \quad (14)$$

Finally, applying this change of variables to Eq. (9)–Eq. (10) leads to the following linear system of coupled ordinary differential equations

$$\frac{d}{dt} \begin{pmatrix} \xi_{q,p} \\ \eta_{q,p} \end{pmatrix} = L \begin{pmatrix} \xi_{q,p} \\ \eta_{q,p} \end{pmatrix}, \quad (15)$$

where matrix L is a specification of matrix $\mathbf{L}_{\bar{q}, \bar{p}}$ in Eq. (S43), defined as

$$L = \begin{pmatrix} -1 & A\Omega_{\bar{q}, \bar{p}} \\ vB & -v \end{pmatrix} \quad (16)$$

and $\Omega_{\bar{q}, \bar{p}}$ is the function that takes into account the spatial coupling terms of Eq. (9)–Eq. (10) within the hexagonal lattice (in this case, $\Omega_{\bar{q}, \bar{p}} \propto [\mathbf{Q}_{\bar{q}, \bar{p}}]_{12}$, defined by Eq. (S42)). We have then turned Eq. (1)–Eq. (2) into a system of constant-coefficient linear differential equations described by Eq. (15), which has a straightforward family of solutions. For now, however, we focus on the coupling function $\Omega_{\bar{q}, \bar{p}}$, which holds the main mechanisms behind the dynamics of juxtracrine and long-range signalling in our system.

$\Omega_{\bar{q}, \bar{p}}$ varies according to the weighting function ω . Here, $\bar{q} = q/N$ and $\bar{p} = p/M$ define the discrete wavenumbers (Fourier modes) and thus solutions for $0 < \bar{q}, \bar{p} \leq 1$ correspond to patterned solutions with corresponding pattern wavelengths $(1/\bar{q}, 1/\bar{p})$. We assume that connections between cells depend only on their relative positions in the lattice (Fig. 1(b)) and therefore, for a sender cell s in position (j, k) and a receiver cell r in position (j', k') , we set $\omega(s_{j,k}, r_{j',k'}) \equiv \omega(j' - j, k' - k) = \omega(\Delta j, \Delta k)$. Hence, $\Omega_{\bar{q}, \bar{p}}$ is, in general, given by

$$\Omega_{\bar{q}, \bar{p}} = \sum_{\Delta j, \Delta k \in S} \omega(\Delta j, \Delta k) e^{2\pi i(\bar{q}\Delta j + \bar{p}\Delta k)}, \quad (17)$$

where $\Delta j, \Delta k \in S$ where $S = \{(j', k') \mid (j', k') \neq (j, k)\}$. Now, if we assume connections are symmetric, i.e., $\omega(\Delta j, \Delta k) = \omega(-\Delta j, -\Delta k)$, we have, by Example 1.1 in SN1,

$$\Omega_{\bar{q}, \bar{p}} = \sum_{\Delta j, \Delta k \in S} \omega(\Delta j, \Delta k) \cos(2\pi(\bar{q}\Delta j + \bar{p}\Delta k)). \quad (18)$$

The diagonalisation of L leads to the temporal eigenvalues

$$\lambda_{\bar{q}, \bar{p}}^{\pm} = \frac{1}{2} \left[-(1 + v) \pm \sqrt{(1 + v)^2 - 4v(1 - AB\Omega_{\bar{q}, \bar{p}})} \right]. \quad (19)$$

Then, since $v > 0$, $\lambda_{\bar{q}, \bar{p}}^+$ is a positive real number if and only if $AB\Omega_{\bar{q}, \bar{p}} > 1$. A and B are the slopes of the feedback functions f and g at the homogeneous steady state and $|AB|$ is defined as the feedback strength. If $|AB| = 0$, then the homogeneous solution is linearly stable, $\text{Re}(\lambda_{\bar{q}, \bar{p}}^\pm) < 0$, and thus no periodic pattern is expected to emerge. On the other hand, the feedback strength has to be sufficiently high for patterns to arise, that is, $|AB| > |1/\Omega_{\min}|$, where Ω_{\min} denotes the minimum of the real function $\Omega_{\bar{q}, \bar{p}}$, so that $\text{Re}(\lambda_{\bar{q}, \bar{p}}^+)$ is maximal. With $A > 0$, $B < 0$ and assuming $\Omega_{\min} < 0$, we expect patterned solutions provided

$$AB < \frac{1}{\Omega_{\min}}. \quad (20)$$

In particular, this feedback is controlled by the tuple (a, b, h, k) as follows

$$A = f'(g(n^*)) = \frac{akd^{*k-1}}{(a + d^{*k})^2} \quad (21)$$

$$B = g'(n^*) = -\frac{bhn^{*h-1}}{(1 + bn^{*h})^2}, \quad (22)$$

where, again, (n^*, d^*) is the homogeneous steady state, $r_t = 1/a$ is the trans-interactions strength and b is the ligand inhibition strength. (n^*, d^*) can be found by setting $\langle d_i \rangle = d_i$ and finding the intersection of the nullclines $n_i = f(d_i)$ and $d_i = g(n_i)$. Assuming for convenience $h = k$, this can be rewritten as

$$n^* = f(g(n^*)) \quad (23)$$

$$d^* = g(n^*), \quad (24)$$

which can be numerically solved for each triple (h, r_t, b) in the parameter space. Such a solution, together with Eq. (20), defines the discrete analogues of Turing spaces consisting of $r_t - b = h$ parameter regions where spontaneous patterns occur. Outside such regions, pattern formation is not expected, since all of the linear modes have negative growth rates.

We now explore different weighting functions to capture the effects of juxtacrine signalling and protrusions, and discuss what features of ω affect Ω_{\min} . We recall that ω determines the family of systems Eq. (1)–Eq. (2) via the weighting dynamics defined by Eq. (6)–Eq. (8).

For a given cell on a hexagonal lattice, we denote the closest ring of order $k \in \mathbb{N}_0$ by R_k , such that R_0 is the cell itself, R_1 are its 6 neighbouring cells, R_2 is the ring of 12 second-neighbour cells, and so forth. Notice that $|R_k| = 6k$ ($k > 0$). We further expand the definition of S in SN1 by defining S_k as the relative index set of cells in R_k (according to Fig. 1(b)), that is,

$$\left\{ \begin{array}{l} S_0 = \{(0, 0)\} \\ S_1 = \{(\pm 1, 0), (0, \pm 1), \pm(1, 1)\} \\ S_2 = \{(0, \pm 2), (\pm 2, 0), \pm(1, -1), \\ \quad \pm(1, 2), \pm(2, 1), \pm(2, 2)\} \\ \vdots \end{array} \right. \quad (25)$$

This notation will be used throughout this work. Notice that such a definition can be ambiguous in different contexts, as discussed in Remark 1.2 (SN1).

3. Results

3.1. Juxtacrine signalling and simplistic protrusions

For juxtacrine signalling on a hexagonal lattice, without protrusions, we set

$$\omega_J(\Delta j, \Delta k) = \begin{cases} \frac{1}{6} & \text{if } (\Delta j, \Delta k) \in S_1, \\ 0 & \text{otherwise,} \end{cases} \quad (26)$$

so that

$$\Omega_{\bar{q}, \bar{p}} = \frac{1}{3} [\cos(2\pi\bar{q}) + \cos(2\pi\bar{p}) + \cos(2\pi(\bar{q} + \bar{p}))]. \quad (27)$$

Notice that $\Omega_{\bar{q}, \bar{p}}$ takes discrete values within the interval $[-0.5, 1]$. The modes that minimise Eq. (27) are those for which N and M are multiples of 3, thus $(\bar{q}, \bar{p}) \in \{(1/3, 1/3), (2/3, 2/3)\}$ and a pattern with wavelength 3 along the main directions of the hexagonal lattice emerges, provided $AB < -2$. In general, and depending on the initial conditions, such patterns may yield 1, 2 or 3 different cell types, as discussed in more detail below.

Considering protrusions, we first look at the more straightforward case where only the first ring of 12 non-neighbouring cells, R_2 , is reached by protrusions. Here, signalling is weighted laterally by Eq. (26) and on R_2 by

$$\omega_P(\Delta j, \Delta k) = \begin{cases} \frac{1}{12} & \text{if } (\Delta j, \Delta k) \in S_2, \\ 0 & \text{otherwise.} \end{cases} \quad (28)$$

Figs. 1(c)–1(f) show the observable patterns for different values of ϵ , with initial conditions near the homogeneous steady state, obtained by solving Eq. (23)–Eq. (24). Notice that the limit case $\epsilon = 1$ has the extreme feature of no juxtacrine signalling, hence the small clusters of Delta-expressing cells in Fig. 1(f). Even for small values of ϵ , sparse patterns are evident.

We may then weight each signalling contribution with a factor $\epsilon > 0$ and define the combined weighting function $\omega = (1 - \epsilon)\omega_J + \epsilon\omega_P$. Using this leads to

$$\begin{aligned} \Omega_{\bar{q}, \bar{p}} = & \frac{(1 - \epsilon)}{3} [\cos(2\pi\bar{q}) + \cos(2\pi\bar{p}) + \cos(2\pi(\bar{q} + \bar{p}))] \\ & + \frac{\epsilon}{6} \left[\cos(4\pi\bar{q}) + \cos(2\pi(\bar{p} - \bar{q})) + \cos(4\pi\bar{p}) \right. \\ & \quad + \cos(2\pi(2\bar{q} + \bar{p})) + \cos(2\pi(\bar{q} + 2\bar{p})) \\ & \quad \left. + \cos(4\pi(\bar{q} + \bar{p})) \right]. \end{aligned} \quad (29)$$

In this case, minimising $\Omega_{\bar{q}, \bar{p}}$ is trickier and therefore we consider a numerical approach. For different values of the long-range signalling strength ϵ , Fig. 2(a) shows the change of $1/|\Omega_{\min}|$ for increasing values of ϵ . Notice that $\Omega_{\max} = 1$ for all ϵ . Equal juxtacrine-protrusion weighting occurs when $\epsilon = 2/3$ ($\Omega_{\min}(2/3) \simeq -0.24$). For each ϵ , the number of modes varies, as seen in Fig. 2(b). Notice that $\Omega_{\bar{q}, \bar{p}} = \Omega_{1-\bar{q}, 1-\bar{p}}$ and, in fact, $\Omega_{\bar{q}, \bar{p}}$ is symmetric with respect to the planes $\bar{q} = \bar{p}$ and $\bar{q} = 1 - \bar{p}$ for all ϵ . An interesting observation is that at around $\epsilon = 0.4$ there are a total of 8 minimising modes, contrasting to the single pair of modes for $\epsilon < 0.4$ and the 6 distinct modes for $\epsilon > 0.4$ (Figs. 2(d)–2(f), Video S1). The bifurcation observed in Fig. 2(b) at $\epsilon = 0.4$ is predicted independently of the Hill functions, and can be mathematically shown by solving, for ϵ ,

$$\Omega_{\frac{1}{3}, \frac{1}{3}}(\epsilon) = \Omega_{\bar{q}, \bar{p}}(\epsilon) \quad (30)$$

and a minimising pair $(\bar{q}, \bar{p}) \notin \{(1/3, 1/3), (2/3, 2/3)\}$ (see SN1 for details). Figs. 2(g)–2(i) show some of the simulations for corresponding values of ϵ .

As discussed before, the critical wave numbers maximise the real part of the temporal eigenvectors. Equivalently, Fig. 2(c) shows $\max_{\bar{q}, \bar{p}} \text{Re}(\lambda_{\bar{q}, \bar{p}}^\pm)$ as a function of the relative weight parameter ϵ , corresponding to the critical $AB = 1/(\max_\epsilon \Omega_{\min}) \simeq -5.207$. Here, $\max_{\bar{q}, \bar{p}} (\text{Re}(\lambda_{\bar{q}, \bar{p}}^\pm)) > 0$ for all ϵ , and thus patterns are expected to emerge with the maximising wavelength modes. As suggested by Eq. (21)–Eq. (24), we may go a step further and work out the specific parameter regions for which $|AB|$ yields pattern formation. The phase diagrams in Fig. 3 (Video S2) represent the regions in the $r_t - b$ plane such that $AB < 1/\Omega_{\min}(\epsilon)$, or more specifically,

$$n^{*1-h} d^{*1-k} ((1 + bn^{*h})(a + d^{*k}))^2 < -abhk\Omega_{\min}(\epsilon) \quad (31)$$

for different values of Ω_{\min} and corresponding ϵ . The ϵ -Collier model is robust with respect to the pair (r_t, b) , corresponding to the trans-interactions strength and ligand inhibition strength parameters, respectively. Increasing ϵ from zero initially reduces the size of the discrete

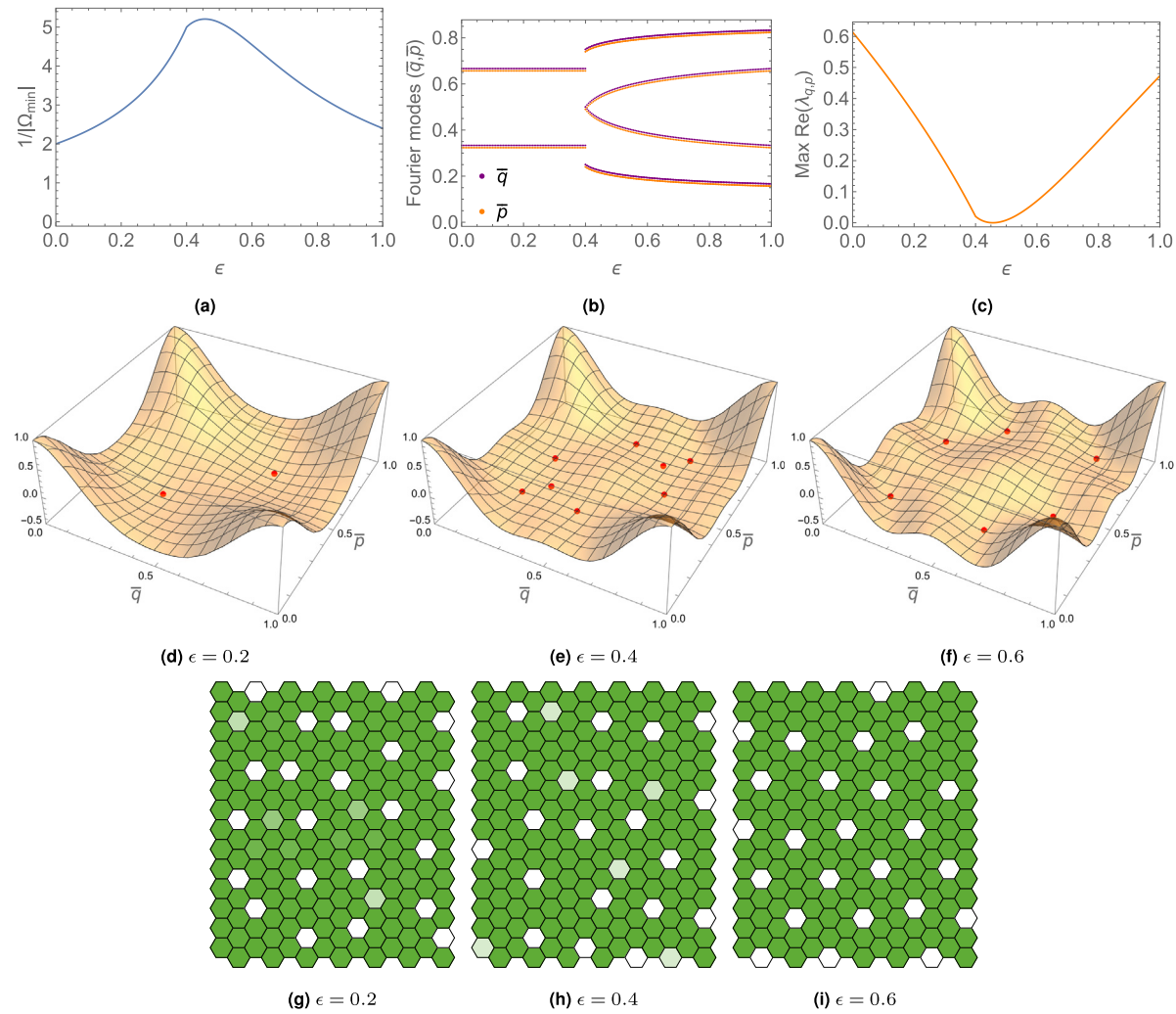


Fig. 2. Coupling dynamics of simplistic protrusions as functions of ϵ .

(a) $1/|\Omega_{\min}|$. In this case, $(\bar{q}, \bar{p})|_{\epsilon=0} \in \{(1/3, 1/3), (2/3, 2/3)\}$ and $\max_{\epsilon} \Omega_{\min} \approx -0.192$. (b) Plot of the fastest growing modes (\bar{q}, \bar{p}) . \bar{q} (purple) and \bar{p} (orange, artificially shifted) have identical plots. (c) Maximum value of $\text{Re}(\lambda_{\bar{q},\bar{p}}^{\pm})$ as function of ϵ , with $AB = 1/(\max_{\epsilon} \Omega_{\min}) \approx -5.207$. (d–f) Plot of $\Omega_{\bar{q},\bar{p}}$ and respective minimising modes (in red). (g–i) Simulations on a 14×14 lattice for different values of ϵ . Parameters similar to Fig. 1 (see Table 1 in Supplementary Note 3).

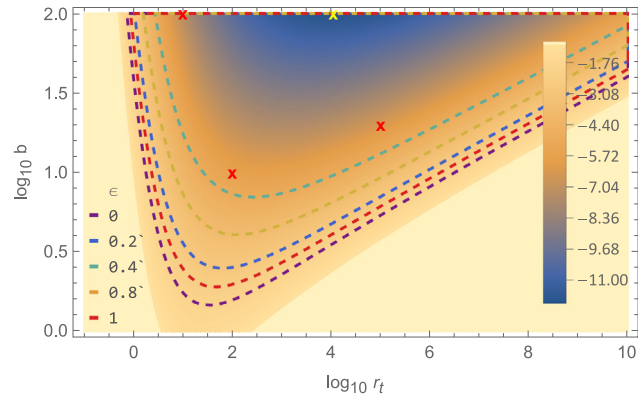


Fig. 3. Phase diagrams.

Log-log contour plot of AB as a function of r_t, b . The regions delimited by the dashed lines indicate the Turing spaces where spontaneous pattern formation occurs ($AB < 1/\Omega_{\min}(\epsilon)$), for each $\epsilon \in \{0, 0.2, 0.4, 0.8, 1\}$. Here, $h = k = 6$. In this region, $\min_{r_t, b} AB \approx -11.986$ at $(r_t, b) \approx (10^{4.04}, 10^2)$ (yellow cross). The purple line corresponds to $AB = -2$ ($\epsilon = 0$). Red crosses indicate the critical points $(r_t, b) \in \{(10, 10^2), (10^2, 10), (10^5, 10^{1.3})\}$. Parameter values are shown in Table 1.

Turing space, in which patterning occurs, followed by an increase after intermediate values of ϵ ($\Omega_{\min}(\epsilon)$ has a maximiser at $\epsilon \approx 0.455$), which is in accordance with the monotonicity change of $1/|\Omega_{\min}|$ (Fig. 2(a)). Note that Turing spaces for different values of ϵ are strictly contained sets, via Eq. (31). In the region $(r_t, b) \in [10^{-1}, 10^{10}] \times [10^0, 10^2]$, patterns emerge for any ϵ , since there are always non-empty Turing spaces ($\min_{r_t, b} AB \approx -11.986 < -5.207 \approx 1/\max_{\epsilon} \Omega_{\min}$). As discussed below, we are interested in the dynamics near bifurcations, where LSA is expected to better predict pattern selection. In particular, we highlight three critical points $(r_t, b) \in \{(10, 10^2), (10^2, 10), (10^5, 10^{1.3})\}$ (red crosses in Fig. 3), for later reference.

Patterning timing is also affected by relative weighting. To measure it, we define a constraint that ensures that the overall change in activity across the lattice does not exceed a certain limit. This can be interpreted as a control mechanism that prevents rapid and drastic changes in Delta activity levels, which could be indicative of unstable or erratic behaviour in the system. We define patterning time as the instant t for which

$$\frac{1}{NM} \sum_{j,k} |d_{j,k}(t) - d_{j,k}(t-1)| \leq \bar{d} \quad (32)$$

holds, for some threshold \bar{d} . With $\bar{d} \approx 0.001$, Fig. S5 shows that patterning converges fast for different ranges of ϵ depending on the critical points. On 14×14 lattices, patterning is slower around $0.35 <$

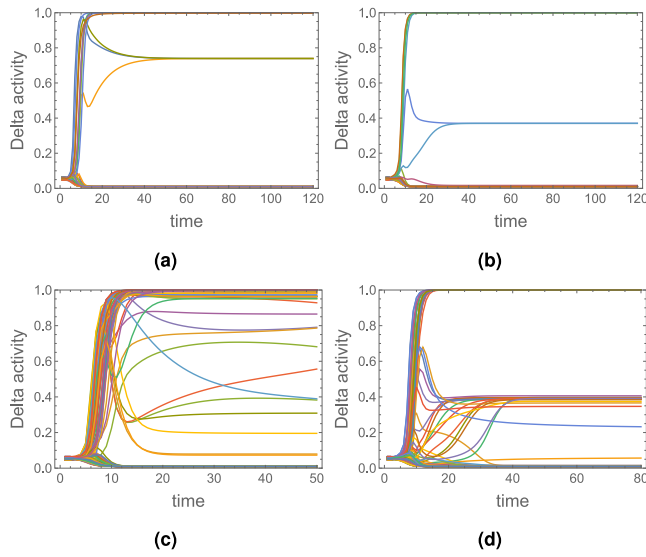


Fig. 4. Dynamics at critical ϵ values.

Delta activity dynamics on (a–b) 6×6 and (c–d) 14×14 periodic lattice, for (a,c) $\epsilon \approx 0.09$, and (b,d) $\epsilon \approx 0.78$. Patterns with multiple cell types emerge for critical values of ϵ .

$\epsilon < 0.55$. In particular, the peak around $\epsilon = 0.4$ is consistent with the dynamics predicted by LSA and $\max \operatorname{Re}(\lambda_{\bar{q}, \bar{p}}^{\pm})$, in Fig. 2(c). Naturally, other refined patterning criteria are conceivable. Our argument is merely an illustration of the predictive power of LSA.

3.2. Multiple cell types

For a narrow range of ϵ values, alternative steady state solutions that include more than two cell types (based on Delta levels) are possible. This effect is observable at both ends of the ϵ spectrum, defining thresholds of pattern selection. To two decimal places, for $\epsilon \approx 0.09$ and $\epsilon \approx 0.78$, 6×6 periodic lattices yield approximately 3 different cell types (Figs. 4(a)–4(b)). For 14×14 lattices, we get a gradient of cell types (Figs. 4(c)–4(d)). Whether some of these solutions eventually converge to others, reducing the number of distinct cell types, is not known. The definition of a cell type is therefore ambiguous and, for larger timescales, processes such as proneural positive feedback or cell proliferation take over, rendering the subject of long-term pattern resolution purely academic. Nonetheless, we believe this effect to be noteworthy.

3.3. Long and oriented protrusions

A possible first extension is to consider the effects of longer or oriented protrusions. Examples of applications regarding this type of long-range signalling can be found in studies of the stripe and spot patterns observed in the skin of zebrafish and pearl danio, respectively [3,23,24].

In [18], a general weighting function was considered to account for protrusion length and orientation. Here, we adapt such a framework by focusing only on the protrusion weighting component ω_{p_g} , given by

$$\omega_{p_g}(\Delta j, \Delta m) = \begin{cases} \omega^* e^{-\sigma_1(d_{s,r} - \hat{d})^2} e^{\sigma_2 \cos(\alpha(\theta_{s,r} - \hat{\theta}))} & \text{if } 1 < d_{s,r} \leq p_\ell \\ & \text{and } |\theta_{s,r}| \geq p_\theta, \\ 0 & \text{otherwise,} \end{cases} \quad (33)$$

where $d_{s,r}$ and $\theta_{s,r} \in (-\pi, \pi]$ are defined as the relative distance and the angular bearing between the signalling and receiving cells, respectively. $\sigma_1, \sigma_2, \hat{d}, \hat{\theta}$ and α are parameters that control the shape and form of

the weighting function, and ω^* is the normalising coefficient implicitly defined by Eq. (7). Furthermore, p_ℓ is the maximum protrusion length and p_θ is an angle bound.

We assume $d_{s,r}$ is the same for each cell in R_k , $k \geq 2$, and thus we may rewrite it, using our previous index notation, as a function of $(\Delta j, \Delta m)$

$$d_{s,r} \equiv d_{s,r}(\Delta j, \Delta m) = k, \text{ if } (\Delta j, \Delta m) \in S_k, \quad (34)$$

which yields $1 < k \leq p_\ell$. Notice that Δm replaces Δk in Fig. 1(b) to avoid confusion with the index of S_k . Eq. (34) is equivalent to the hexagonal-Manhattan distance d_H defined in Remark 1.2 (SN1). Notice also that, with $p_\ell = 2$, $p_\theta = 0$, $\sigma_{1,2} = 0$ and $\omega^* = 1/12$, we recover the R_2 weighting function ω_P given by Eq. (28). We set, in this case, $\omega = (1-\epsilon)\omega_J + \epsilon\omega_{p_g}$.

We focus only on the case of longer protrusions and thus we impose radial symmetry by taking $\sigma_2 = 0$, $p_\theta = 0$ (cases with $\sigma_2 > 0$ lead to axial and polarised signalling systems, as discussed in [18]). Intuitively, σ_1 represents the strength of ligand density decay with distance. In the following, we assume long-range signalling strength to decrease as a function of $d_{s,r}$ and therefore take $\hat{d} = d_{s,r}(\Delta j, \Delta m)|_{(\Delta j, \Delta m) \in R_2} = 2$ and $\sigma_1 > 0$. Hence Eq. (33) simplifies to

$$\omega_{p_g}(\Delta j, \Delta m) = \begin{cases} \omega^* e^{-\sigma_1(d_{s,r}(\Delta j, \Delta m) - 2)^2} & \text{if } 1 < d_{s,r} \leq p_\ell, \\ 0 & \text{otherwise,} \end{cases} \quad (35)$$

where, from Eq. (7),

$$\overline{\omega_{p_g}}(p_\ell, \sigma_1) \equiv \frac{1}{\omega^*} \quad (36)$$

$$= \sum_{(\Delta j, \Delta m) \in \bigcup_{k=2}^{p_\ell} S_k} e^{-\sigma_1(d_{s,r}(\Delta j, \Delta m) - 2)^2} \quad (37)$$

$$= 6 \sum_{k=2}^{p_\ell} k e^{-\sigma_1(k-2)^2}. \quad (38)$$

Under the assumption that protrusions may reach up to R_4 ($p_\ell = 4$), we have that, as an example, $\overline{\omega_{p_g}}(4, \sigma_1) = 12 + 18e^{-\sigma_1} + 24e^{-4\sigma_1}$. For different values of σ_1 , Fig. 5(d) shows the minimal feedback strength required for patterning, derived from $\Omega_{\bar{q}, \bar{p}}$. The case $\sigma_1 = 0$ yields equal R_k ($2 \leq k \leq 4$) weighting and thus $\omega^* = 1/|\bigcup_{k=2}^{p_\ell} R_k| = 1/54$, in this case (Figs. 5(a)–5(c)). As $\sigma_1 \rightarrow \infty$, $\omega^* \rightarrow 1/12$ and we recover the dynamics for R_2 protrusions (Fig. 5(e)). Figs. 6(a)–6(c) show simulations for different values of p_ℓ . Interestingly, the pattern wavelengths for $p_\ell = 4$ are not correctly predicted by LSA, as seen by comparing the minimisers of Fig. 5(c) with the simulation in Fig. 6(c). For this value of p_ℓ , the minimising modes remain unchanged for a wider range of ϵ .

Considering bounded protrusions significantly alters the coupling function and symmetry may be broken. Interesting pattern may arise in this case when $\epsilon = 1$, especially regarding the emergence of clustering effects or zebrafish-type patterns, as shown in Figs. 6(d)–6(e) and discussed in some of the work by Binshtok and Sprinzak [25], Kondo et al. [24], Moreira and Deutsch [26].

3.4. Stochastic protrusions

One way of generalising the weighting function ω is to consider some level of randomness in protrusion-cell signalling. Previous studies have suggested that pattern regularity and refinement can be greatly improved by considering dynamic lifespan-based protrusions [9]. Here, we extend such an approach to the ϵ -Collier model on the R_2 ring.

Depending on the protrusion type and level of biological detail, different stochastic models may be implemented. For example, in the case of the eukaryotic flagellum [27] and stereocilia [28], the length evolution can be studied using a master equation with length-dependent rates of protrusion attachment and detachment. For such systems, the length fluctuations can be mapped onto an Ornstein–Uhlenbeck process. In other work, the length dynamics of bacterial protrusions (*pili*) have

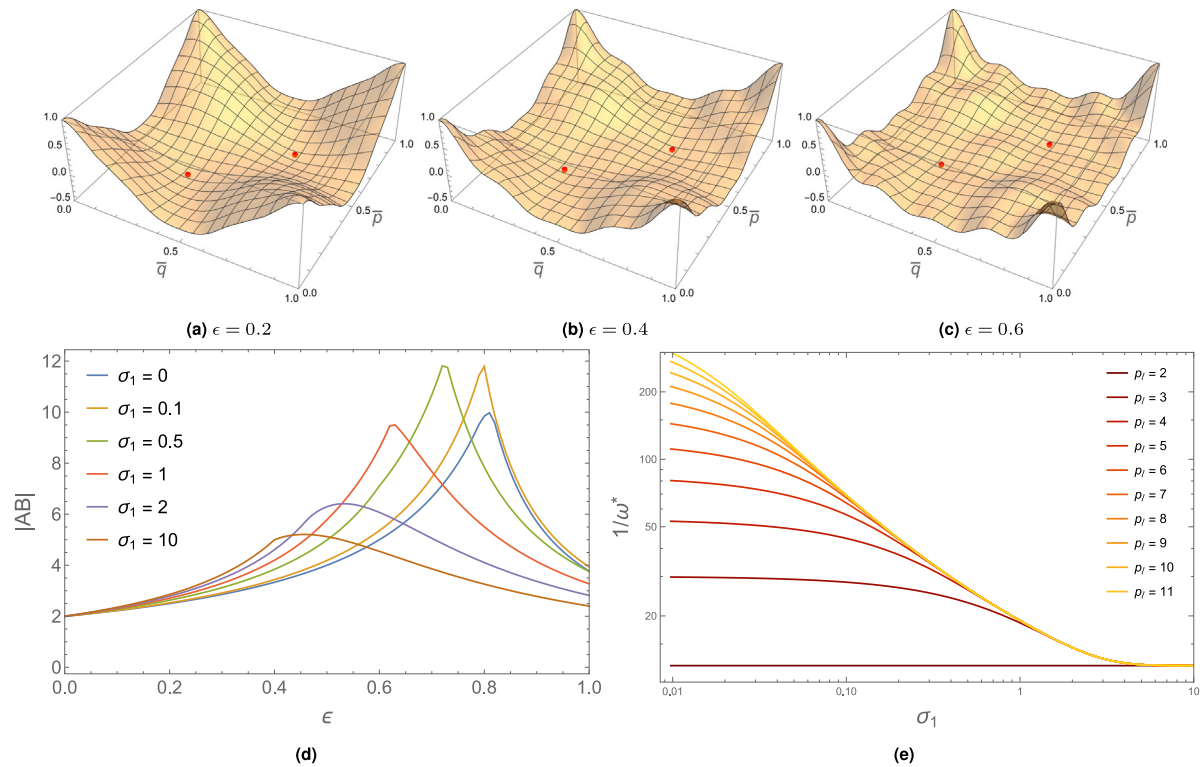


Fig. 5. Coupling dynamics of long protrusions as functions of ϵ .

(a–c) Plot of $\Omega_{q,p}$ and respective minimising modes (in red) with $\sigma_1 = 0$. Wavier plots are observable due to the more complex nature of the weighting function, considering $p_\ell = 4$. (d) Critical $|AB|$ for different values of σ_1 , given by $|1/\Omega_{\min}|$, with $p_\ell = 4$. (e) $1/\omega^*$ as a function of p_ℓ and σ_1 . $\omega^* \rightarrow 1/12$ as $\sigma_1 \rightarrow \infty$. Parameters are shown in Table 1.

been described by a three-state Markov process [29]. Further details on the physics of filopodial protrusions can be found in [20,30] and an extensive discussion on length control of long cell protrusions of various types was presented in [31].

Here, however, we assume isotropic protrusions and consider dynamic binding and unbinding of filopodia to non-neighbouring cells throughout the simulation. The lifespan of protrusions is determined by birth and death rates, p_b and p_d , respectively. These correspond to the attachment and detachment rates of protrusions to non-neighbouring cells. Within a short time interval Δt , a link is formed between a cell and one of its second neighbours with probability $p_b \Delta t$. Such a link is destroyed with probability $p_d \Delta t$. This leads to the formulation of a continuous-time telegraph process [32–35] with rates p_b and p_d . This process is also known as a dichotomic or two-valued Markov process. In the following, we first present well-known results on telegraph processes, followed by the application to our case.

From stochastic theory, the general telegraph process is defined as a memoryless continuous-time stochastic process that has two distinct values. If the two possible values that a random variable $X(t)$ can take are x_1 and x_2 , then the process can be described by the following master equations

$$\partial_t P(x_1, t|x, t_0) = -\gamma_1 P(x_1, t|x, t_0) + \gamma_2 P(x_2, t|x, t_0) \quad (39)$$

$$\partial_t P(x_2, t|x, t_0) = \gamma_1 P(x_1, t|x, t_0) - \gamma_2 P(x_2, t|x, t_0), \quad (40)$$

where γ_1 is the transition rate from state x_1 to state x_2 and γ_2 is the transition rate from state x_2 to state x_1 . In this case, x_1 represents the state where a protrusion is absent and x_2 where it is present.

We are now interested in studying the asymptotic dynamics of the telegraph process, approximating its discrete realisations to a Bernoulli process, given a suitable condition on the realisation timescales. With $\Delta t \equiv t - t_0 \gg (\gamma_1 + \gamma_2)^{-1}$, the solution approaches a stationary distribution \mathbf{P}_s given by

$$\mathbf{P}_s \equiv \lim_{\Delta t \gg (\gamma_1 + \gamma_2)^{-1}} \mathbf{P}(t) = \frac{1}{\gamma_1 + \gamma_2} \begin{pmatrix} \gamma_2 \\ \gamma_1 \end{pmatrix}, \quad (41)$$

where $\mathbf{P} = (P(x_1, t|x, t_0), P(x_2, t|x, t_0))^T$. The stationary average is then given by

$$\langle X \rangle_s = \frac{x_1 \gamma_2 + x_2 \gamma_1}{\gamma_1 + \gamma_2}. \quad (42)$$

In our case, we have $\gamma_1 = p_b$, $\gamma_2 = p_d$, $x_1 = 0$ and $x_2 = 1$. Hence, in the limit where $\Delta t \gg (p_b + p_d)^{-1}$, the probability of finding a protrusion is $p_b/(p_b + p_d)$. We may then treat such a process as a Bernoulli process with probability $p_b/(p_b + p_d)$. In other words, if the timescale at which we make the observation is longer than the inverse of the event rates, we may expect the process to be memoryless every time we observe, describing a Bernoulli process.

For each k in R_2 (cells reached by protrusions), we extend the ϵ -Collier model to account for these stochastic dynamics by defining the following random variables

$$\tilde{\epsilon}_k \stackrel{\text{iid}}{\sim} \text{Bern} \left(\frac{p_b}{p_b + p_d} \right). \quad (43)$$

We assume that neighbouring R_1 cells are always linked, with weight $(1-\epsilon)/6$, and R_2 cells are linked with stochastic weight $\epsilon \tilde{\epsilon}_k / 12$. At each time step, the stochastic coupling term is then given by

$$\langle \tilde{d}_i \rangle(t) = \frac{1-\epsilon}{6} \sum_{j \in R_1} d_j(t) + \frac{\epsilon}{12} \sum_{k \in R_2} d_k(t) \tilde{\epsilon}_k, \quad (44)$$

where the second term is a sum of weighted i.i.d. Bernoulli distributions. Note that \tilde{d}_i here should not be confused with the homogeneous state perturbation introduced in other sections. One of the key aspects of having dynamic protrusions is the possibility of pattern refinement over time. As suggested in [9], we define the coefficient of variation, ζ_V , of a pattern as the ratio between the standard deviation and mean of the distances from each SOP cell to its 6 closest SOP cells. This coefficient yields a measure of the global order of the emergent pattern, which we then track for different values of (p_b, p_d) , as seen in Fig. 7(a). The case $(p_b, p_d) = (10, 3.5)$ is particularly interesting as the pattern converges to ideal cell packing ($\zeta_V = 0$) at around $t = 390$ (Fig. 7(e)).

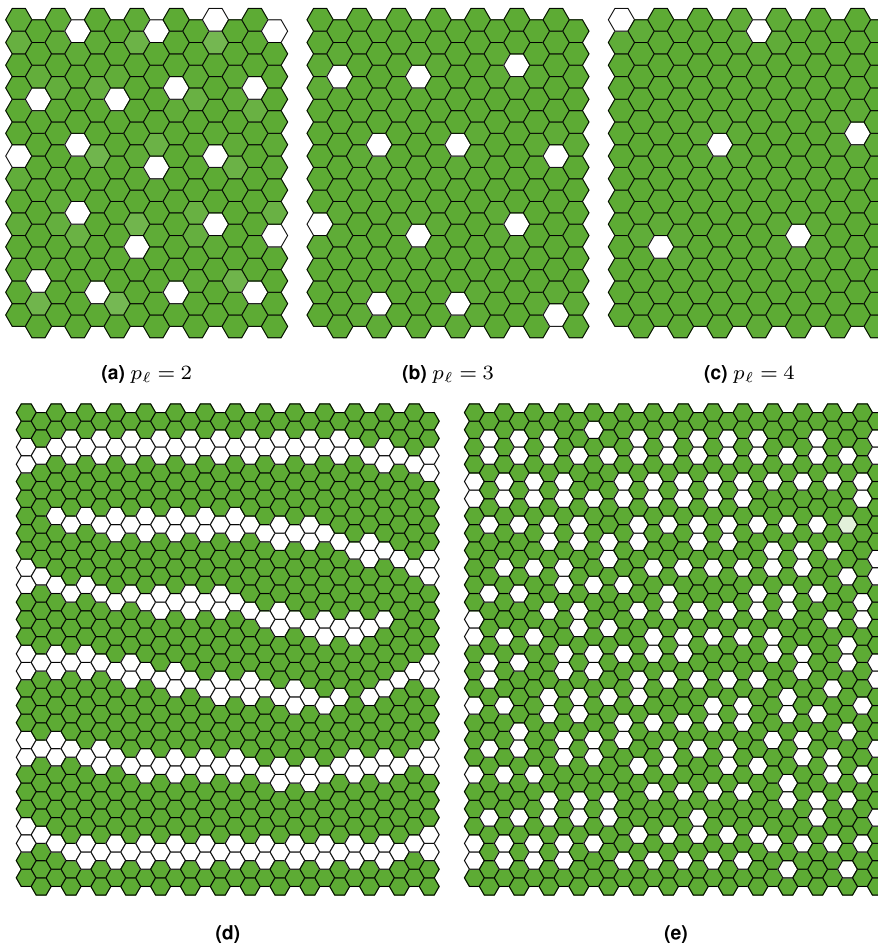


Fig. 6. Patterning with long and oriented protrusions.

(a–c) Simulations on a 14×14 lattice for different values of p_ℓ . Here, $\epsilon = 0.6$ and $h = k = 6$. (d–e) Bounded protrusions may lead to other patterns, relevant to other applications. Here, (d) $(\epsilon, p_\ell, p_\theta) = (1, 3, \pi/3)$, and (e) $(\epsilon, p_\ell, p_\theta) = (0.8, 2, \pi/4)$.

Some patterns only stabilise once optimal packing is attained, depending on the tissue dimensions. For a periodic tissue whose dimensions are multiples of 14, which guarantees optimal R_2 -signal sparse patterning is possible (notice that 14×7 would also work), once the coefficient of variation is minimised, patterning does stabilise. In many cases, given enough time, the stable R_3 pattern is obtained after gradual refinement determined by p_b and p_d . In a perfectly refined pattern, one should expect $\zeta_V = 0$, which means each SOP cell is surrounded in R_3 by 6 other equally spaced SOP cells (Fig. 7(e), Video S3).

It should be noted that the simulations shown in Fig. 7 are all isolated examples corresponding to single realisations. Although the purpose of this study is to identify p_b and p_d such that pattern refinement is achieved, the complex relation between such rates to guarantee convergence to the refined pattern may be hinted at by a thorough stochastic analysis, which is beyond the scope of this work.

Remarkably, if we look at the extreme case of sudden removal of protrusions (from the refined state), we find that such a state is stable under purely juxtacrine lateral inhibition (Fig. 7(e)). This is similar to taking $\epsilon = 0$ after pattern stabilisation. Patterns of such wavelength contrast with the ones predicted by LSA, but they do not contradict pattern selection under consideration of nonlinear terms [19], as discussed below.

Considering different approaches to noise-driven protrusions might help in better understanding the role of stochastic effects in patterning and refinement. For instance, avoiding the Bernoulli approximation on the Markov-type protrusion dynamics could hint at a more realistic description of filopodium behaviour and consequently pattern formation.

Noise-mediated filopodium reach and orientation have been studied in [9]. Cellular automaton models have also been used to explain sparse and more complex patterns [10]. Dichotomous noise has also been applied in Langevin dynamics, in a broader scenario [36].

A natural alternative to this source of noise, is to study the role of intrinsic noise, driven by Langevin dynamics [37,38]. In the case of morphogen-mediated patterning of gene expression, intrinsic noise has proven to affect timescale dynamics of bistable switches [39]. Stochastic effects were shown to accelerate juxtacrine pattern formation and alternative lateral inhibition models [40] were found to be robust to intrinsic noise [14]. Statistical properties of protein concentration in gene-regulated networks were more generally discussed in [41]. In the particular case of Notch-Delta and protrusions, a recent implementation of Gillespie's Stochastic Simulation Algorithm (SSA) [38] was discussed in [42], for a more convoluted signalling system, following the model by Hadjivasiliou et al. [11]. Here, the authors interpreted the relevant concentrations at each cell as absolute molecular counts at some fixed system volume.

3.5. Robustness and pattern selection

We now explore how Fourier analysis describes pattern selection under LSA. Again, we discuss robustness to changes in two of the main parameters in the ϵ -Collier model: the Hill function switch parameters, given by the trans-interactions strength $r_t = 1/a$ and the ligand inhibition strength b . We study the convergence to the desired pattern with long-range signalling for different values of a and b . Here, we consider

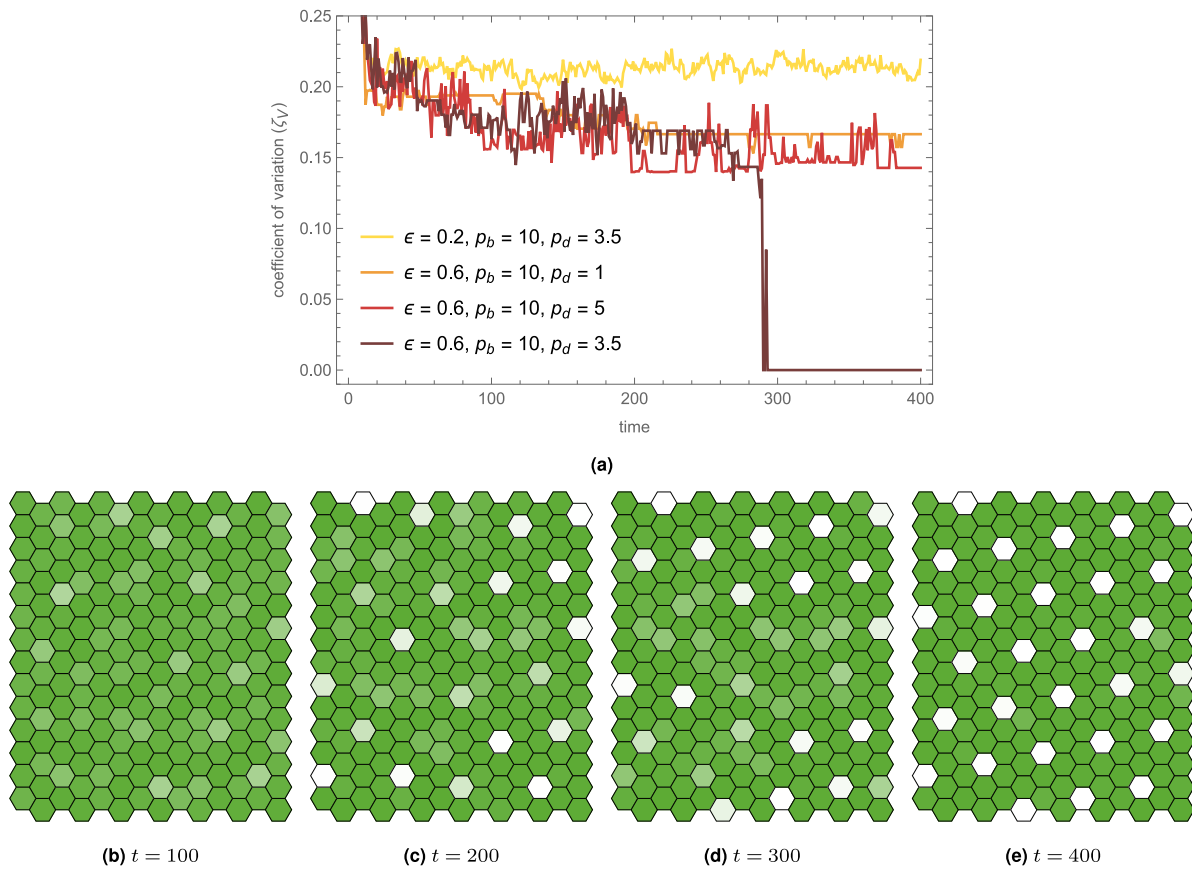


Fig. 7. Dynamics of stochastic protrusions.

(a) Stochastic behaviour of the coefficient of variation ζ_V in spacing between nearest Delta-expressing cells. (b–e) Pattern refinement may take a long time to stabilise. Once reaching the refined state at $t = 400$, the pattern hardly changes. The final pattern is also stable under no protrusions. Here, $\epsilon = 0.6$, $p_b = 10$ and $p_d = 3.5$. Other parameter values are shown in Table 1.

protrusions acting on the R_2 ring. In a system with two variables per cell like the linearised system

$$\frac{d}{dt} \tilde{n}_i = A \langle \tilde{d}_i \rangle - \tilde{n}_i \quad (45)$$

$$\frac{d}{dt} \tilde{d}_i = vB \tilde{n}_i - v \tilde{d}_i \quad (46)$$

the characteristic polynomial is of second order. As a consequence, each couple (\bar{q}, \bar{p}) has two eigenvectors and eigenvalues. We then have that the solution of the linearised problem is given by

$$\begin{pmatrix} \tilde{n}_{j,k}(t) \\ \tilde{d}_{j,k}(t) \end{pmatrix} = \sum_{q=1}^N \sum_{p=1}^M \mathbf{A}(\bar{q}, \bar{p}) e^{2\pi i (\bar{q}j + \bar{p}k)}, \quad (47)$$

where

$$\mathbf{A}(\bar{q}, \bar{p}) \equiv C_{\bar{q}, \bar{p}}^+ e^{\lambda_{\bar{q}, \bar{p}}^+ t} \mathbf{v}_{\bar{q}, \bar{p}}^+ + C_{\bar{q}, \bar{p}}^- e^{\lambda_{\bar{q}, \bar{p}}^- t} \mathbf{v}_{\bar{q}, \bar{p}}^-, \quad (48)$$

and where $\mathbf{v}_{\bar{q}, \bar{p}}^\pm$ and $\lambda_{\bar{q}, \bar{p}}^\pm$ are the eigenvectors and eigenvalues associated to (\bar{q}, \bar{p}) , respectively. $C_{\bar{q}, \bar{p}}^+$ and $C_{\bar{q}, \bar{p}}^-$ are constants depending on the initial conditions of the problem. In the case that at least one family of modes (\bar{q}, \bar{p}) grows exponentially fast, it linearly destabilises the homogeneous solution and this family dominates over the rest, giving rise to a periodic pattern with the (\bar{q}, \bar{p}) -wavenumbers. At such critical modes, we have that the eigenvalue with the largest real part and respective eigenvector are given, as functions of ϵ , by

$$\lambda^*(\epsilon) = \frac{1}{2}(-1 + v) + \sqrt{(1 + v)^2 - 4v(1 - AB\Omega_{\min}(\epsilon))} \quad (49)$$

$$v^*(\epsilon) = \left(\frac{1}{2}(v - 1) + \sqrt{(1 + v)^2 - 4v(1 - AB\Omega_{\min}(\epsilon))} \right) / vB. \quad (50)$$

Hence, for large t , the dominant pattern is a superposition of modes with periodicity determined by (\bar{q}, \bar{p}) and ϵ . Thus, for each family of

critical modes \mathcal{W} , the solutions in Eq. (47) asymptotically satisfy

$$\begin{pmatrix} \tilde{n}_{j,k} \\ \tilde{d}_{j,k} \end{pmatrix} \simeq \mathbf{v}^* e^{\lambda^* t} \sum_{(\bar{q}, \bar{p}) \in \mathcal{W}} C_{\bar{q}, \bar{p}}^+ e^{2\pi i (\bar{q}j + \bar{p}k)}, \quad (51)$$

where λ^* , \mathbf{v}^* and \mathcal{W} are all functions of ϵ . It is then clear that the long term behaviour of this solution is dependent on the amplitudes of the Fourier components in Eq. (51), which in turn depend on the initial conditions of the problem. In fact, since $\mathbf{v}^* e^{\lambda^* t}$ is independent of (\bar{q}, \bar{p}) and $|e^{2\pi i (\bar{q}j + \bar{p}k)}| = 1$, the relative amplitude is given by $C_{\bar{q}, \bar{p}}^+$, which is implicitly determined by

$$C_{\bar{q}, \bar{p}}^+ \mathbf{v}_{\bar{q}, \bar{p}}^+ + C_{\bar{q}, \bar{p}}^- \mathbf{v}_{\bar{q}, \bar{p}}^- = \begin{pmatrix} \xi_{q,p}(0) \\ \eta_{q,p}(0) \end{pmatrix} \quad (52)$$

$$= \frac{1}{NM} \sum_{j=1}^N \sum_{k=1}^M \begin{pmatrix} \tilde{n}_{j,k}(0) \\ \tilde{d}_{j,k}(0) \end{pmatrix} e^{-2\pi i (\bar{q}j + \bar{p}k)}. \quad (53)$$

Hence, depending on the choice of the initial conditions and consequently, $C_{\bar{q}, \bar{p}}^+$, the long-term behaviour of the solution could yield different patterns and cell types. Similar to the analysis in [19], the generic pattern predicted by linear stability analysis might yield more than two cell types, depending on the choices of $C_{\bar{q}, \bar{p}}^+$. Away from the bifurcation, cells usually opt for one of two possible fates, where, approximately, $(n, d) \in \{(0, 1), (1, 0)\}$. Therefore nonlinear effects are expected to play a role in determining the number of cell types. In particular, our model is robust because the final pattern of cell differentiation is not affected by the specific form of the Hill functions, as long as the feedback between cells is strong enough, similar to the lateral inhibition case ($\epsilon = 0$). Fig. 8 shows the pattern selection with corresponding fastest growing modes for different values of ϵ and $C_{\bar{q}, \bar{p}}^+ = 1$. From the vector in Eq. (51), we simply plot the real part of

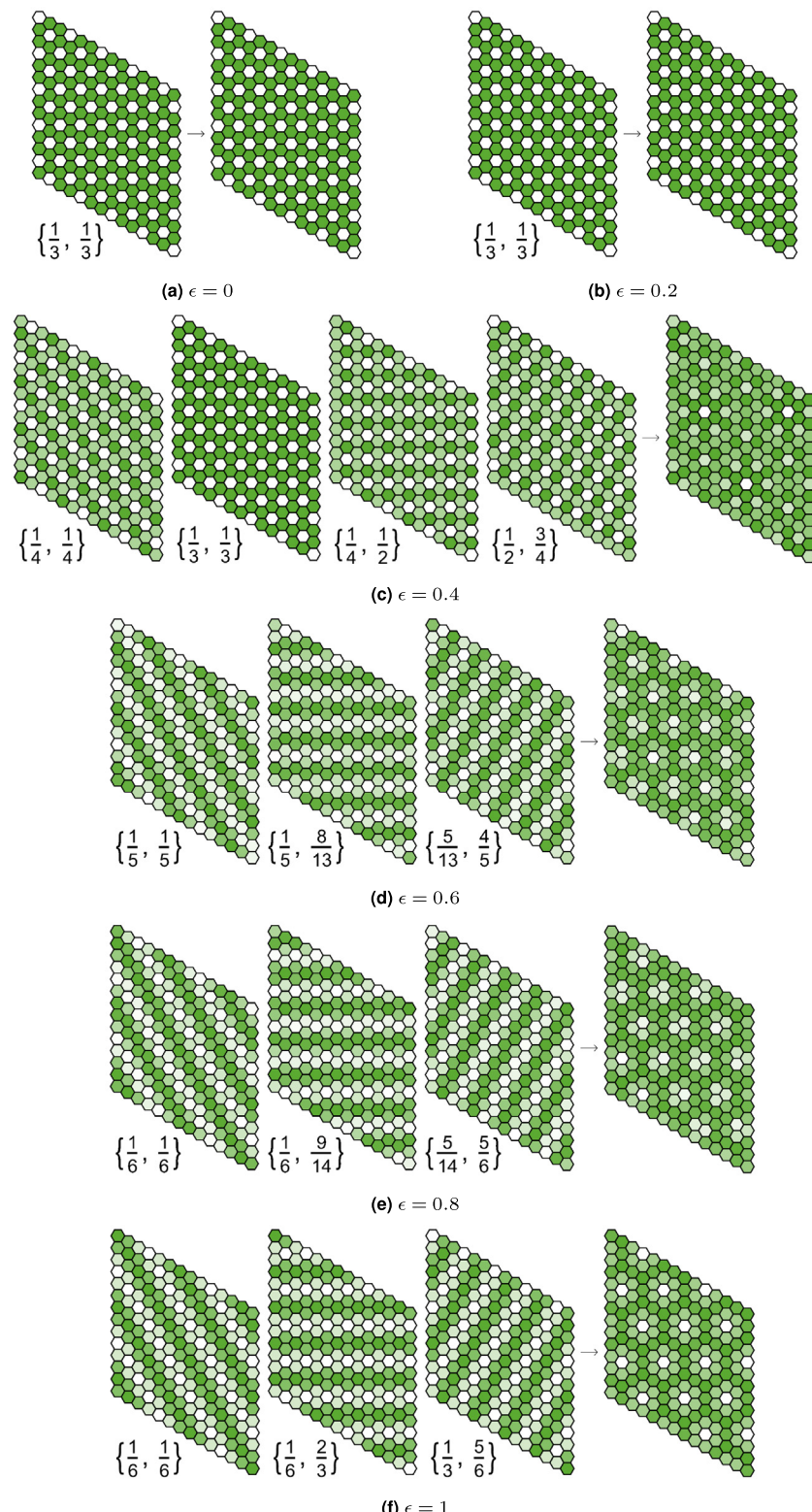


Fig. 8. Pattern selection via LSA: asymptotic solutions.

Eq. (51) decomposes the asymptotic solution to the linearised system in terms corresponding to different minimising modes (\bar{q}, \bar{p}) . Each solution term is represented on the left of each of the subfigures (a–f), for different values of ϵ , while their linearly combined solution is on the right. Due to symmetry, the pattern observed for each single mode (\bar{q}, \bar{p}) is the same for $(1 - \bar{q}, 1 - \bar{p})$ and thus we omit half of the single mode patterns. Here, $C_{\bar{q}, \bar{p}}^+ = 1 \forall (\bar{q}, \bar{p})$. The modes in (d) and (e) are rational approximations of the real values, as explained in the main text. Other parameter values are shown in Table 1.

the normalised sum values of its second term, corresponding to Delta activity (determining the opacity of each white cell). When necessary, and to illustrate the nature of the pattern, we provide rational approximations of the real values of the minimising (\bar{q}, \bar{p}) -wavenumbers. While

we do not expect, from LSA alone, to capture the main mechanisms required to explain longer wavelength patterns, pattern selection close to the bifurcations in Fig. 3 may be predicted and explained by such an analysis. For further results, a nonlinear approach is then required

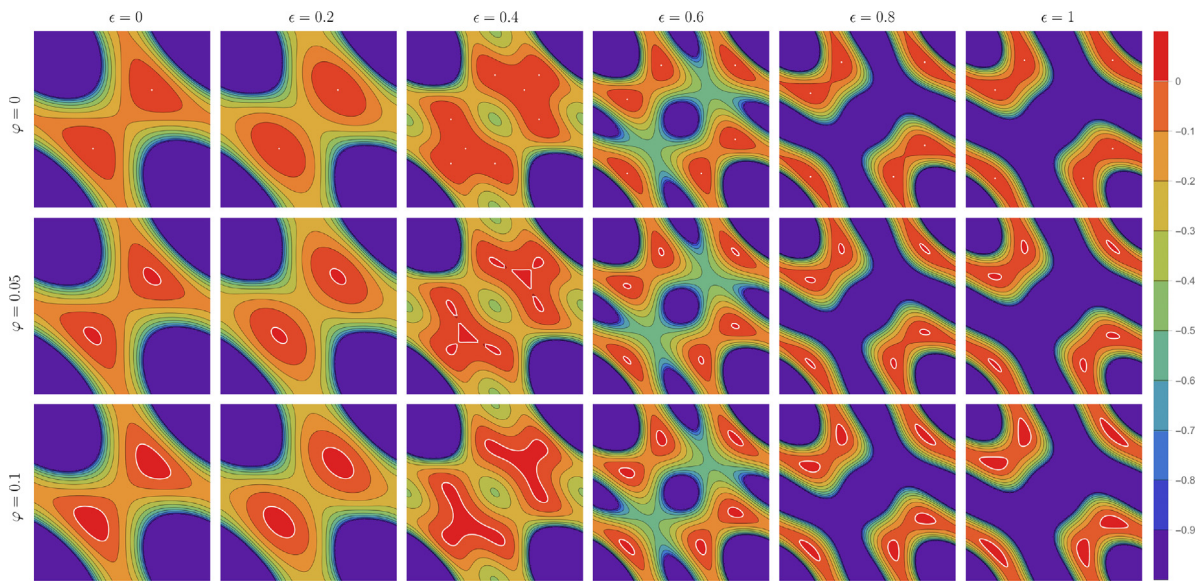


Fig. 9. Wavenumber level set bifurcation.

Contour plots of $\text{Re}(\lambda_{\bar{q},\bar{p}}^+)$ as a function of ϵ and φ , satisfying $AB - \varphi \leq 1/\Omega_{\min}(\epsilon)$. Here, we consider the critical feedback strength AB for each ϵ , so that, at $\varphi = 0$, $AB = 1/\Omega_{\min}(\epsilon)$. White contours are defined by $\text{Re}(\lambda_{\bar{q},\bar{p}}^+) = 0$. For $\varphi = 0$, these correspond to the minimisers \mathcal{W} . As φ increases, initially disconnected and progressively larger wavenumber regions where $\text{Re}(\lambda_{\bar{q},\bar{p}}^+) > 0$ emerge, corresponding to different level sets of the coupling function and determining instability robustness.

to extract some more information on the dynamics of such systems and pattern selection. We discuss both research avenues next.

3.5.1. Bifurcation analysis

In the context of studying long-range Notch-Delta signalling via protrusions in the ϵ -Collier model, both theoretical and numerical approaches can provide valuable insights into the system's behaviour near bifurcation points. While theoretical approaches such as centre manifold and normal form theory [43–46] can be useful, we focus on a numerical bifurcation analysis, which offers a more practical and computationally efficient way to study the system's dynamics [47,48]. By analysing the real part of the eigenvalues of the decoupled linearised system, we can gain insights into the bifurcation dynamics. In the case of Notch-Delta signalling, previous work has revealed intricate bifurcation dynamics in lateral inhibition models without protrusions, in a three-equation system [15,40,49]. These studies have revealed the presence of Hopf bifurcations, helping to understand the conditions that lead to oscillatory and stationary patterns in the signalling dynamics. In other work, also in a three-equation context, pitchfork bifurcations were shown to occur over critical values of Notch and Delta production rates, where antihexagon patterns emerged [50]. Bifurcations under long-range signalling were also studied by Chen et al. [51], to show that the neural pattern in *Ciona* may be explained and reproduced by a Notch-mediated gradient of long-range signalling. In our case, when $v = 1$, the eigenvalues of the decoupled linearised system are given by

$$\lambda_{\bar{q},\bar{p}}^{\pm} = -1 \pm \sqrt{\Omega_b}. \quad (54)$$

We can then study the bifurcation dynamics by varying the parameter $\Omega_b \equiv AB\Omega_{\bar{q},\bar{p}}$. The real part of the eigenvalues determines the stability of the fixed point and the nature of the bifurcation. As we vary Ω_b , we can observe the following bifurcation behaviour: When $\Omega_b < 1$, both eigenvalues have negative real parts, which indicates a stable fixed point. No bifurcation occurs in this region. When $\Omega_b = 1$, one of the eigenvalues has a real part equal to zero, marking a transition point where a bifurcation may occur. When $\Omega_b > 1$, one eigenvalue has a positive real part, and the other has a negative real part. This scenario corresponds to an unstable fixed point and indicates the presence of a saddle-node bifurcation.

While this holds in the frequency domain, stability around non-hyperbolic equilibria in the full nonlinear system is more complex. To

better understand the dynamics around the bifurcation, we can plot the real part of the eigenvalues for varying neighbouring values of AB , with fixed critical $\Omega_{\bar{q},\bar{p}}$ (Fig. 9). This approach allows us to visualise the changes in the stability of the system as the bifurcation parameter AB varies, providing insights into the nature of the bifurcation and the behaviour of the system near the critical point. By analysing the real part of the eigenvalues for different values of AB , we can identify the transition point where a bifurcation occurs.

In the region near the bifurcation, we can virtually decrease the region of instability, approaching the bifurcation from an unstable region. In the context of pattern and wavenumber selection, this analysis is particularly useful, since it allows us to improve the predictive power of linear stability analysis, making it more likely that our numerical simulations will accurately capture the dynamics of the system near the critical point. In Fig. 10, we show numerical simulations of the ϵ -Collier model around multiple bifurcation points, where LSA is expected to predict pattern selection. In particular, we consider triples (r_t, b, ϵ) near the bifurcations defined in Fig. 3. We take $(r_t, b) \in \{(10, 10^2), (10^2, 10), (10^5, 10^{1.3})\}$.

In the vicinity of these parameter values, LSA effectively discerns the intrinsic dynamics governing pattern selection within the ϵ -Collier model. For instance, while small ϵ values appear to ensure sparse patterning away from these points, numerical simulations are consistent with wavelength selection via LSA for $\epsilon < 0.4$. Under these conditions, we anticipate short-ranged 3-period patterns to occur along the primary hexagonal axes, as illustrated in the first two columns of Fig. 10. As ϵ surpasses the bifurcation threshold ($\epsilon = 0.4$), the expression of directional clustering (stripes) and multiple cell types becomes increasingly dominant, owing to the diminishing strength of lateral inhibition in comparison to long-range signalling. This is also predicted by the linear analysis.

3.6. Multiscale methods

In addition to numerical bifurcation analysis, multiple scales methods can be used to further investigate the weakly nonlinear dynamics of the system [52–55]. These techniques involve the analysis of different timescales and spatial scales in the model, allowing for the identification of slow and fast dynamics and their interactions. Such an approach

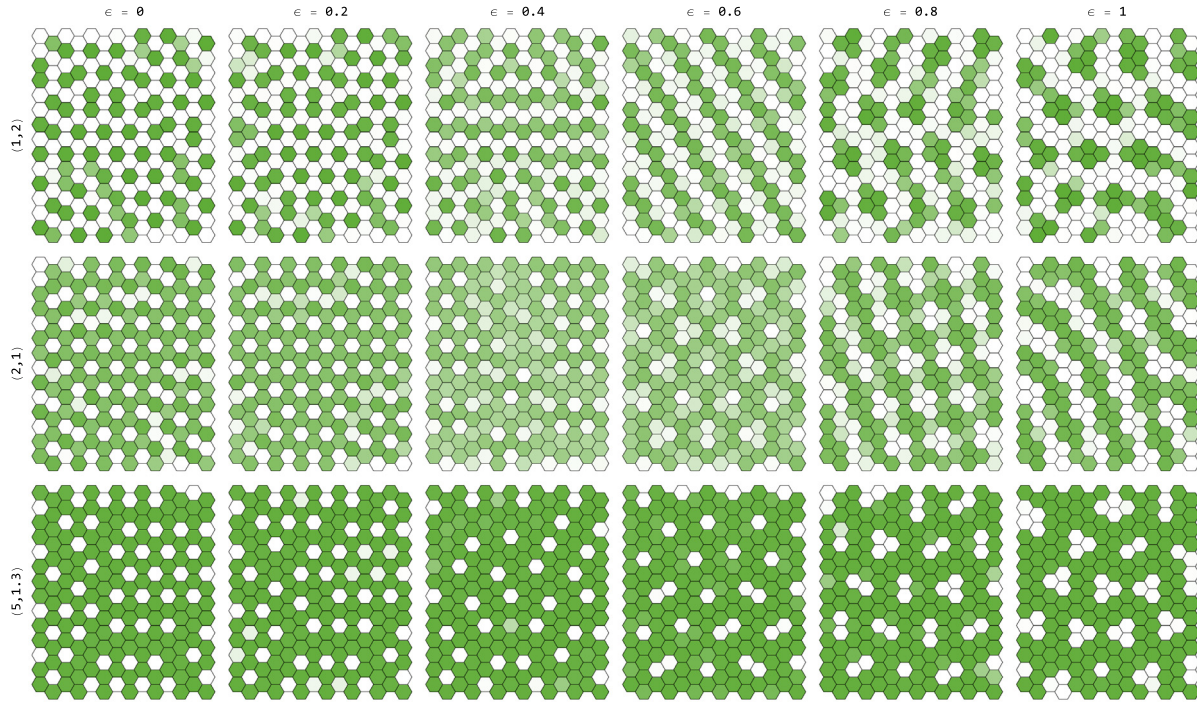


Fig. 10. Numerical simulations close to bifurcations.

Different patterns emerge around bifurcations. Here, we take $h = k = 6$ and consider three different parameter values near the bifurcations in Fig. 3, for varying ϵ : $(r_t, b) \in \{(10, 10^2), (10^2, 10), (10^5, 10^{1.3})\}$ ($\log_{10} r_t, \log_{10} b$ is shown on the y-axis). For $\epsilon < 0.4$, 3-period patterns are expected to emerge along the two main hexagonal axes, as predicted by LSA. In particular, around $(r_t, b) \simeq (10, 10^2)$, antihexagon patterns seem to emerge, as discussed in [50]. For intermediate values of ϵ ($0.4 < \epsilon < 0.6$), high trans-interactions strength (r_t) seems to ensure the robustness of sparser patterns, even close to a bifurcation, as seen at $(r_t, b) \simeq (10^5, 10^{1.3})$. Clustering of Delta-expressing cells becomes gradually more evident as ϵ increases, supported by the relatively large long-range signalling weighting, compared to lateral-inhibition. Multiple cell types are expected across a wide range of ϵ values, due to high-level branching of steady state solutions. r_t and b are correlated with φ via Eq. (21)–Eq. (22). Opacity levels are normalised at each simulation, and therefore white does not necessarily correspond to Delta activity equal to 1. The homogeneous steady states for each parameter pair are shown in Table 1.

can provide valuable insights into the complex behaviour of the long-range Notch-Delta signalling via protrusions, informing experimental studies and contributing to a better understanding of the signalling dynamics in biological systems. We discuss a brief application of such methods to our model, as well as their limitations.

Following Remark 1.1 in SN1, we aim to derive a continuum model upon the discrete model, so that we solve the decoupling issue with standard weakly nonlinear stability analysis (WNSA) on a translationally invariant system (see SN2). To do so, a homogenisation process must be employed. We follow the framework in [56,57]. For a hexagonal arrangement of cells, we denote the distance between cell centres by $\delta \ll 1$, introduce a slowly-varying continuum variable $\mathbf{x} = \delta \mathbf{v}$, $\mathbf{v} \in \mathbb{R}^2$, and express the levels of Delta and Notch activity using the multiscale representation $n_i(t) = n(t, \mathbf{x})$ and $d_i(t) = d(t, \mathbf{x})$, where i represents the fast spatial variable and \mathbf{x} represents the slow spatial variable. Second-order Taylor expanding in two variables leads to

$$d_{i+1}(t) \simeq d(t, \mathbf{x} + \delta \mathbf{v}) \quad (55)$$

$$\simeq d(t, \mathbf{x}) + \delta \nabla_{\mathbf{x}} d(t, \mathbf{x}) \cdot \mathbf{v} + \frac{\delta^2}{2} \mathbf{v}^T \mathbf{H}_d(\mathbf{x}) \mathbf{v}, \quad (56)$$

where $\nabla_{\mathbf{x}}$ and \mathbf{H}_d are the (spatial) gradient and Hessian of d , respectively. We are interested in studying the dynamics of Delta across different directions. Without loss of generality, take the distance between any two adjacent cell centres to be 1. Hence, the relevant directions in our homogenisation correspond to the vectors between cell centres. Namely, with

$$\mathbf{U}_1 = \left\{ \left(\cos\left(\frac{k\pi}{3}\right), \sin\left(\frac{k\pi}{3}\right) \right) \right\}_{1 \leq k \leq 6} \quad (57)$$

$$\mathbf{U}_2 = \left\{ \left(\cos\left(\frac{k\pi}{3} + \frac{\pi}{6}\right), \sin\left(\frac{k\pi}{3} + \frac{\pi}{6}\right) \right) \right\}_{1 \leq k \leq 6}, \quad (58)$$

we define the following sets of vectors:

- First neighbour vectors (R_1): $\mathbf{V}_1 = \mathbf{U}_1$;
- Second neighbour vectors (R_2): $\mathbf{V}_2 = 2\mathbf{U}_1 \cup \sqrt{3}\mathbf{U}_2$.

Due to hexagonal symmetry, we have

$$\sum_{\mathbf{v} \in \mathbf{V}_1} d(t, \mathbf{x} + \delta \mathbf{v}) \simeq 6d(t, \mathbf{x}) + \frac{3\delta^2}{2} \nabla_{\mathbf{x}}^2 d(t, \mathbf{x}) \quad (59)$$

$$\sum_{\mathbf{v} \in \mathbf{V}_2} d(t, \mathbf{x} + \delta \mathbf{v}) \simeq 12d(t, \mathbf{x}) + \frac{21\delta^2}{2} \nabla_{\mathbf{x}}^2 d(t, \mathbf{x}), \quad (60)$$

where $\nabla_{\mathbf{x}}^2$ is the (spatial) Laplacian. Hence,

$$\langle d_i \rangle \simeq \frac{1 - \epsilon}{6} \sum_{\mathbf{v} \in \mathbf{V}_1} d(t, \mathbf{x} + \delta \mathbf{v}) + \frac{\epsilon}{12} \sum_{\mathbf{v} \in \mathbf{V}_2} d(t, \mathbf{x} + \delta \mathbf{v}) \quad (61)$$

$$\simeq d(t, \mathbf{x}) + \delta(\epsilon) \nabla_{\mathbf{x}}^2 d(t, \mathbf{x}) + \mathcal{O}(\delta^4), \quad (62)$$

where $\delta(\epsilon) \equiv \delta^2(2 + 5\epsilon)/8$. The goal is now to study the equations at the timescale on which spatial coupling enters at $\mathcal{O}(\delta)$, which can be achieved with $\tau = \delta t$. Setting $A(t) \equiv \delta(\epsilon)$ in Eq. (S83) yields $b_m = 0, \forall m$ and so, in this case, Eq. (S131)–Eq. (S134) simplify to (see SN2 for full derivation details)

$$\mathbf{0} = \mathbf{J}(\mathbf{u}^*) \mathbf{v}_1 \quad (63)$$

$$\mathbf{0} = \mathbf{J}(\mathbf{u}^*) \mathbf{v}_2 + \frac{1}{2} \begin{pmatrix} \mathbf{v}_1^T \mathbf{H}_1(\mathbf{u}^*) \mathbf{v}_1 \\ \mathbf{v}_1^T \mathbf{H}_2(\mathbf{u}^*) \mathbf{v}_1 \end{pmatrix} \quad (64)$$

$$\mathbf{0} = \mathbf{J}(\mathbf{u}^*) \mathbf{v}_3 + \frac{1}{2} \begin{pmatrix} \mathbf{v}_2^T \mathbf{H}_1(\mathbf{u}^*) \mathbf{v}_1 \\ \mathbf{v}_2^T \mathbf{H}_2(\mathbf{u}^*) \mathbf{v}_1 \end{pmatrix} + \frac{1}{6} (D^3 \mathbf{F})_{\mathbf{u}^*} [(\mathbf{v}_1)^3], \quad (65)$$

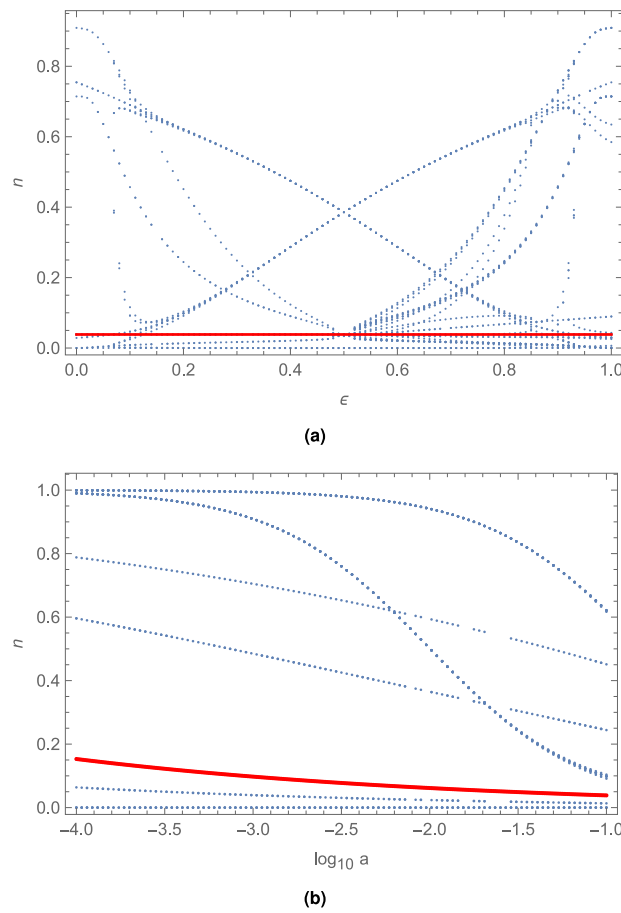


Fig. 11. Bifurcation diagrams in the ϵ -Collier model. Bifurcation diagram for a 5-cell periodic system via the ϵ -Collier model. The homogeneous steady state n^* is shown in red for each case. (a) Steady states n for varying ϵ , with $h = k = 2$, $a = 10^{-1}$, and $b = 10^4$. $n^* \approx 0.03848$, for all ϵ . At $\epsilon = 0.5$, first and second neighbours equally contribute to signalling. (b) Steady states n for varying a , with $\epsilon = 0.2$, $h = k = 2$, and $b = 10^4$.

where $\mathbf{u} \equiv (n, d)$. We are then looking for solutions of the form

$$\mathbf{u}(t) = \mathbf{u}^* + \mathbf{v}_1\delta(\epsilon) + \mathbf{v}_2\delta(\epsilon)^2 + \mathbf{v}_3\delta(\epsilon)^3 + O(\delta^4). \quad (66)$$

The case $\epsilon = 0$ was discussed in [57] for 3-period patterns along the main hexagonal axes. In this case, three distinct cell types were considered. For $\epsilon > 0$, however, there is a dramatic rise in mathematical complexity as a result of the variety of new patterning possibilities. In particular, it becomes challenging to track the perturbations around bifurcations, as these drastically increase in number. To illustrate the complexity induced by long-range signalling, we consider a simplified model along one of the main hexagonal axes. Considering a 5-cell system with periodic boundary conditions (so that R_2 is now a non-overlapping pair of second-neighbours), we plot the bifurcation diagrams under variation of ϵ and a (Fig. 11). Here, we do not distinguish between stable and unstable states, but multiple pitchfork bifurcations are expected from $AB < 1/\Omega_{\min}$. The case $h > 2$ is computationally more demanding to solve and does not invalidate the discussion here. The homogeneous steady states are shown in red. The various branches reveal the difficulty in performing multiscale analysis on our particular system. While 5-period patterns may be expected from linear analysis (Fig. 8(d)), applying multiscale methods to our wavelength selection is, in general, a challenging task, which adds to the contrast between lateral-inhibition models and a model of long-range signalling such as the ϵ -Collier model.

Overall, multiple scale analysis is a powerful technique for studying systems with distinct temporal or spatial scales. However, its application to systems with numerous bifurcations is debatable, due to

the complexity of bifurcations, sensitivity to initial conditions, and parameter dependence, which is more pronounced in a model like ours. Bifurcations introduce intricate behaviours that blur the boundaries between scales, while the sensitivity to initial conditions and parameter dependence makes it difficult to determine appropriate scales for analysis. To overcome these limitations, future work could focus on designing adaptive multiscale techniques that dynamically adjust to evolving system dynamics, in general lattices and signalling networks [58,59].

In the supplementary information, and motivated by reaction-diffusion systems, we explore a possible application of WNSA to patterning derived from long-range signalling, and discuss its limitations in our system's coupling dynamics [17,60–62]. Compared to LSA, and as detailed in SN2, decoupling seems mathematically unfeasible in the case of translationally invariant Notch-Delta signalling systems, given the complexity generated by the higher-order terms. Any decoupling methodology as systematic as the linear case seems to be out of reach within our framework.

4. Discussion

In this work, we have outlined some of the main tools for analysing a general long-range signalling model. We developed such a model by taking a relative signalling approach. Long-range signalling via filopodia is weighted by a parameter ϵ , while the juxtacrine contribution is weighted by $1 - \epsilon$. This constitutes the ϵ -Collier model, understood as a long-range extension of the original Collier model [19]. We found that sparser patterns on periodic hexagonal lattices are robust and tend to emerge for a wide range of ϵ values. To comprehend the linear effects of long-range signalling, we first employed a linear stability analysis for generally coupled and translationally invariant systems (SN1), followed by a direct application to the ϵ -Collier model. We explored various protrusion modelling frameworks, including short- and long-range protrusions, and stochastic protrusion dynamics. We discovered that patterning timing is highly dependent on ϵ , as supported by our stability analysis.

Overall, LSA proved to be a useful tool for identifying the fastest-growing modes under Fourier analysis, and, in addition to solely juxtacrine models, LSA was able to predict short and sparse patterning across a broad range of ϵ values. In particular, we examined parameters closer to the bifurcation point at which the homogeneous state becomes linearly unstable (dashed lines in Fig. 3). Here, it was anticipated that the model behaves more linearly; hence, LSA may match the simulation outcomes better, which we confirmed with numerical simulations for specific critical bifurcation neighbourhoods. If this does not occur, it may indicate we are near a subcritical bifurcation (as opposed to a supercritical one), and when a subcritical bifurcation occurs, LSA does not necessarily predict the patterning outcome [63,64]. Away from critical points, nonlinear effects play a significant role in sparse pattern selection and alternative methods were discussed, including multiple scales methods and weakly nonlinear stability analysis inspired by reaction-diffusion literature.

Multiple scales methods have proven to be indispensable tools for investigating Notch-Delta signalling, as they facilitate the analysis of the complex interplay between molecular interactions and cellular behaviour across spatial and temporal scales [56,57]. These methods elucidate the intricate dynamics of signalling networks, which can become mathematically intractable as the network expands, and demonstrated by the increasing number of steady-state bifurcations in the case of the ϵ -Collier model. Furthermore, these methods often involve bridging the gap between discrete and continuum descriptions of cellular processes, taking into account stochastic fluctuations, reaction-diffusion kinetics, and the spatial organisation of signalling components. The continuum approach requires a thorough rethinking of the ϵ parameter, which determines the relative signalling strength between lateral inhibition and protrusion-based signalling.

Motivated by the multiscale approach, we devised a framework for weakly nonlinear stability analysis in order to achieve expanded

qualitative conclusions on wavelength selection in Fourier-transformed coupling functions. Specifically, we presented the main methodology behind a potential framework for WNSA of translationally invariant Notch-Delta systems. We expanded well-known reaction-diffusion techniques to coupled spatially discrete systems, such as the ϵ -Collier model on a periodic hexagonal lattice, by considering harmonic-based Landau-type solutions. We found that the decoupling mechanism in translationally invariant systems appears impractical in WNSA.

Ultimately, this work outlines a framework for understanding pattern formation in relatively general long-range signalling systems, highlighting some of the primary mathematical challenges in such a theory and indicating possible generalisations and future research avenues, in the context of both linear and weakly nonlinear methodologies. Furthermore, the single-parameter adaptability of the ϵ -Collier model encompasses a whole family of long-range signalling phenomena, which can be adjusted for a variety of modelling approaches. Our findings have significant implications for understanding the behaviour of natural systems, such as the SOP patterning in the fly notum and the skin patterns of different *danio* species, where sparse patterns are observed. In particular, the ϵ -Collier model will be adapted in a subsequent publication to study the emergence of sensory organ precursors on the wing pouch of *Drosophila melanogaster* during the late third instar, which is a crucial aspect of wing development.

The fact that such patterns arise for a broad range of ϵ values suggests that the interplay between long-range signalling and juxtacline contribution plays a key role in cell fate commitment. Understanding its underlying dynamics could be useful for developing new strategies to monitor or control patterning in biological systems, such as tissue engineering or regenerative medicine.

5. Computational methods

5.1. Simulations

All simulations were performed using *Interactive Epithelium* (IEp), a *Wolfram Mathematica* tool for hybrid Notch-Delta epithelial signalling and patterning simulations. IEp aims to provide a practical tool for testing parameter robustness while simulating the dynamics of the Notch-Delta signalling pathway in an epithelium. Table 1 in Supplementary Note 3 contains the precise parameter values for the simulation plots shown in this work.

5.2. Code availability

The source code and data that were used to develop the main conclusions and analyses presented in this work are available on the following repository hosted on GitHub: <https://github.com/fberkemeier/Notch-Delta-Coupling.git>. The relevant video simulations can also be found in this repository. Previous versions are available upon request. For any comments/suggestions, as well as copyright issues, please contact fp409@cam.ac.uk.

Declaration of competing interest

The authors declare that they have no known competing financial interests or personal relationships that could have appeared to influence the work reported in this paper.

Data availability

No external data is required. See *Code availability* for further details.

Acknowledgments

We would like to thank Drs. M. Dalwadi, P. Pearce, R. Pérez-Carrasco, and G. Paci, and Profs. Y. Mao, B. Baum and N. Monk for their helpful discussions and comments that greatly improved the manuscript. This research was made possible by a UCL Studentship Award from the Department of Mathematics and the Leverhulme Trust Research Project Grant RPG-2022-028.

Appendix A. Supplementary data

Supplementary material related to this article can be found online at <https://doi.org/10.1016/j.mbs.2023.109012>.

References

- [1] S.M. Cohen, Long-range signalling by touch, *Nature* 426 (6966) (2003) 503–504.
- [2] C. De Joussineau, J. Soule, M. Martin, C. Anguille, P. Montcourier, D. Alexandre, Delta-promoted filopodia mediate long-range lateral inhibition in *drosophila*, *Nature* 426 (6966) (2003) 555–559.
- [3] H. Hamada, M. Watanabe, H.E. Lau, T. Nishida, T. Hasegawa, D.M. Parichy, S. Kondo, Involvement of delta/notch signaling in zebrafish adult pigment stripe patterning, *Development* 141 (2) (2014) 318–324.
- [4] G.L. Hunter, L. He, N. Perrimon, G. Charras, E. Giniger, B. Baum, A role for actomyosin contractility in notch signalling, *BMC Biol.* 17 (1) (2019) 1–15.
- [5] F.A. Ramírez-Weber, T.B. Kornberg, Cytonemes: cellular processes that project to the principal signaling center in *drosophila* imaginal discs, *Cell* 97 (5) (1999) 599–607.
- [6] A.-C. Gradilla, I. Guerrero, Cytoneme-mediated cell-to-cell signaling during development, *Cell Tissue Res.* 352 (1) (2013) 59–66.
- [7] T.B. Kornberg, S. Roy, Cytonemes as specialized signaling filopodia, *Development* 141 (4) (2014) 729–736.
- [8] N.M. Sherer, W. Mothes, Cytonemes and tunneling nanotubes in cell-cell communication and viral pathogenesis, *Trends Cell Biol.* 18 (9) (2008) 414–420.
- [9] M. Cohen, M. Georgiou, N.L. Stevenson, M. Miodownik, B. Baum, Dynamic filopodia transmit intermittent delta-notch signaling to drive pattern refinement during lateral inhibition, *Dev. Cell* 19 (1) (2010) 78–89.
- [10] M. Cohen, B. Baum, M. Miodownik, The importance of structured noise in the generation of self-organizing tissue patterns through contact-mediated cell-cell signalling, *J. R. Soc. Interface* 8 (59) (2010) 787–798.
- [11] Z. Hadjivasiliou, G.L. Hunter, B. Baum, A new mechanism for spatial pattern formation via lateral and protrusion-mediated lateral signalling, *J. R. Soc. Interface* 13 (124) (2016) 20160484.
- [12] Z. Hadjivasiliou, R.E. Moore, R. McIntosh, G.L. Galea, J.D. Clarke, P. Alexandre, Basal protrusions mediate spatiotemporal patterns of spinal neuron differentiation, *Dev. Cell* 49 (6) (2019) 907–919.
- [13] D.T. Gillespie, The chemical langevin equation, *J. Chem. Phys.* 113 (1) (2000) 297–306.
- [14] T. Rudge, K. Burrage, Effects of intrinsic and extrinsic noise can accelerate juxtacline pattern formation, *Bull. Math. Biol.* 70 (4) (2008) 971–991.
- [15] S.D. Webb, M.R. Owen, Oscillations and patterns in spatially discrete models for developmental intercellular signalling, *J. Math. Biol.* 48 (4) (2004) 444–476.
- [16] B. Zakirov, G. Charalambous, R. Thuret, I.M. Aspalter, K. Van-Vuuren, T. Mead, K. Harrington, E.R. Regan, S.P. Herbert, K. Bentley, Active perception during angiogenesis: filopodia speed up notch selection of tip cells in silico and in vivo, *Phil. Trans. R. Soc. B* 376 (1821) (2021) 20190753.
- [17] A. Turing, The chemical basis of morphogenesis, *Phil. Trans. R. Soc. B* 237 (641) (1952) 37–72.
- [18] G. Vasilopoulos, K.J. Painter, Pattern formation in discrete cell tissues under long range filopodia-based direct cell to cell contact, *Math. Biosci.* 273 (2016) 1–15.
- [19] J.R. Collier, N.A. Monk, P.K. Maini, J.H. Lewis, Pattern formation by lateral inhibition with feedback: a mathematical model of delta-notch intercellular signalling, *J. Theoret. Biol.* 183 (4) (1996) 429–446.
- [20] A. Mogilner, B. Rubinstein, The physics of filopodial protrusion, *Biophys. J.* 89 (2) (2005) 782–795.
- [21] P. Formosa-Jordan, M. Ibañes, Diffusible ligand and lateral inhibition dynamics for pattern formation, *J. Stat. Mech. Theory Exp.* 2009 (03) (2009) P03019.
- [22] J. Murray, Mathematical Biology II: Spatial Models and Biomedical Applications, Springer New York, 2001.
- [23] D.S. Eom, E.J. Bain, L.B. Patterson, M.E. Grout, D.M. Parichy, Long-distance communication by specialized cellular projections during pigment pattern development and evolution, *Elife* 4 (2015) e12401.
- [24] S. Kondo, M. Watanabe, S. Miyazawa, Studies of turing pattern formation in zebrafish skin, *Phil. Trans. R. Soc. A* 379 (2213) (2021) 20200274.
- [25] U. Binshtok, D. Sprinzak, Modeling the notch response, in: Molecular Mechanisms of Notch Signaling, Springer, 2018, pp. 79–98.

- [26] J. Moreira, A. Deutsch, Pigment pattern formation in zebrafish during late larval stages: A model based on local interactions, *Dev. Dyn. Off Pub. Am. Assoc. Anatom.* 232 (1) (2005) 33–42.
- [27] W.F. Marshall, J.L. Rosenbaum, Intraflagellar transport balances continuous turnover of outer doublet microtubules: implications for flagellar length control, *J. Cell Biol.* 155 (3) (2001) 405–414.
- [28] P. Narayanan, P. Chatterton, A. Ikeda, S. Ikeda, D.P. Corey, J.M. Ervasti, B.J. Perrin, Length regulation of mechanosensitive stereocilia depends on very slow actin dynamics and filament-severing proteins, *Nature Commun.* 6 (1) (2015) 1–8.
- [29] M.D. Koch, C. Fei, N.S. Wingreen, J.W. Shaevitz, Z. Gitai, Competitive binding of independent extension and retraction motors explains the quantitative dynamics of type IV pili, *Proc. Natl. Acad. Sci.* 118 (8) (2021) e2014926118.
- [30] S. Patra, D. Chowdhury, Length fluctuations of long cell protrusions: statistics of passage times, random and extremal excursions, 2020, arXiv preprint [arXiv:2008.09851](https://arxiv.org/abs/2008.09851).
- [31] S. Patra, D. Chowdhury, F. Jülicher, Length control of long cell protrusions: rulers, timers and transport, *Phys. Rep.* 987 (2022) 1–51.
- [32] M. Kac, A stochastic model related to the telegrapher's equation, *Rocky Mountain J. Math.* 4 (3) (1974) 497–509.
- [33] I. Bena, C. Van den Broeck, R. Kawai, K. Lindenberg, Nonlinear response with dichotomous noise, *Phys. Rev. E* 66 (4) (2002) 045603.
- [34] A.D. Kolesnik, N. Ratanov, *Telegraph Processes and Option Pricing*, Vol. 204, Springer, 2013.
- [35] O. López, N. Ratanov, On the asymmetric telegraph processes, *J. Appl. Probab.* 51 (2) (2014) 569–589.
- [36] D. Barik, P.K. Ghosh, D.S. Ray, Langevin dynamics with dichotomous noise; direct simulation and applications, *J. Stat. Mech. Theory Exp.* 2006 (03) (2006) P03010.
- [37] D.T. Gillespie, A general method for numerically simulating the stochastic time evolution of coupled chemical reactions, *J. Comput. Phys.* 22 (4) (1976) 403–434.
- [38] D.T. Gillespie, Exact stochastic simulation of coupled chemical reactions, *J. Phys. Chem.* 81 (25) (1977) 2340–2361.
- [39] R. Perez-Carrasco, P. Guerrero, J. Briscoe, K.M. Page, Intrinsic noise profoundly alters the dynamics and steady state of morphogen-controlled bistable genetic switches, *PLoS Comput. Biol.* 12 (10) (2016) e1005154.
- [40] H.J. Wearing, M.R. Owen, J.A. Sherratt, Mathematical modelling of juxtacrine patterning, *Bull. Math. Biol.* 62 (2) (2000) 293–320.
- [41] M. Thattai, A. Van Oudenaarden, Intrinsic noise in gene regulatory networks, *Proc. Natl. Acad. Sci.* 98 (15) (2001) 8614–8619.
- [42] S. Engblom, Stochastic simulation of pattern formation in growing tissue: a multilevel approach, *Bull. Math. Biol.* 81 (8) (2019) 3010–3023.
- [43] S. Wiggins, S. Wiggins, M. Golubitsky, *Introduction To Applied Nonlinear Dynamical Systems and Chaos*, Vol. 2, (3) Springer, 2003.
- [44] Y.A. Kuznetsov, I.A. Kuznetsov, Y. Kuznetsov, *Elements of Applied Bifurcation Theory*, vol. 112, Springer, 1998.
- [45] M. Markakis, P. Douris, An efficient center manifold technique for hopf bifurcation of n-dimensional multi-parameter systems, *Appl. Math. Model.* 50 (2017) 300–313.
- [46] D. Sattinger, Group representation theory, bifurcation theory and pattern formation, *J. Funct. Anal.* 28 (1) (1978) 58–101.
- [47] H.G. Meijer, F. Dercole, B.E. Oldeman, et al., Numerical bifurcation analysis., 2009.
- [48] W. Marszalek, H. Podhaisky, J. Sadecki, Computing two-parameter bifurcation diagrams for oscillating circuits and systems, *IEEE Access* 7 (2019) 115829–115835.
- [49] M.R. Owen, J.A. Sherratt, Mathematical modelling of juxtacrine cell signalling, *Math. Biosci.* 153 (2) (1998) 125–150.
- [50] E. Teomy, D.A. Kessler, H. Levine, Ordered hexagonal patterns via notch-delta signaling, *Phys. Biol.* 18 (6) (2021) 066006.
- [51] J.S. Chen, A.M. Gumbayan, R.W. Zeller, J.M. Mahaffy, An expanded notch-delta model exhibiting long-range patterning and incorporating microRNA regulation, *PLoS Comput. Biol.* 10 (6) (2014) e1003655.
- [52] K. Fujimura, Methods of centre manifold and multiple scales in the theory of weakly nonlinear stability for fluid motions, *Proc. R. Soc. Lond. Ser. A Math. Phys. Eng. Sci.* 434 (1892) (1991) 719–733.
- [53] N.E. Sanchez, The method of multiple scales: asymptotic solutions and normal forms for nonlinear oscillatory problems, *J. Symbolic Comput.* 21 (2) (1996) 245–252.
- [54] A.H. Nayfeh, *Perturbation Methods*, John Wiley & Sons, 2008.
- [55] A. Luongo, On the use of the multiple scale method in solving 'difficult'bifurcation problems, *Math. Mech. Solids* 22 (5) (2017) 988–1004.
- [56] R.D. O'Dea, J.R. King, Multiscale analysis of pattern formation via intercellular signalling, *Math. Biosci.* 231 (2) (2011) 172–185.
- [57] R.D. O'Dea, J.R. King, Continuum limits of pattern formation in hexagonal-cell monolayers, *J. Math. Biol.* 64 (2012) 579–610.
- [58] E. Plahte, Pattern formation in discrete cell lattices, *J. Math. Biol.* 43 (5) (2001) 411–445.
- [59] E. Plahte, L. Øyeaug, Pattern-generating travelling waves in a discrete multicellular system with lateral inhibition, *Physica D* 226 (2) (2007) 117–128.
- [60] J. Stuart, On the non-linear mechanics of wave disturbances in stable and unstable parallel flows part 1. The basic behaviour in plane poiseuille flow, *J. Fluid Mech.* 9 (3) (1960) 353–370.
- [61] J. Watson, On the non-linear mechanics of wave disturbances in stable and unstable parallel flows part 2. The development of a solution for plane poiseuille flow and for plane couette flow, *J. Fluid Mech.* 9 (3) (1960) 371–389.
- [62] D.J. Wollkind, V.S. Manoranjan, L. Zhang, Weakly nonlinear stability analyses of prototype reaction-diffusion model equations, *Siam Rev.* 36 (2) (1994) 176–214.
- [63] J.D. Crawford, Introduction to bifurcation theory, *Rev. Modern Phys.* 63 (4) (1991) 991.
- [64] I. Stefanou, S. Aleivizos, Fundamentals of bifurcation theory and stability analysis, *Instabilities Modeling in Geomechanics* (2016) 31–71.